

Department of Physics and Astronomy

University of Heidelberg

Master thesis

in Physics

submitted by

Alexander Mil

born in Rudnja, Russia

September 2016



# **Design and Implementation of a Versatile Imaging Objective for Imaging of Ultracold Mixtures of Sodium and Lithium**

This Master thesis has been carried out by Mil Alexander

at the

Kirchhoff Institute for Physics

under the supervision of

Prof. Dr. Fred Jendrzejewski



## Abstract

This thesis presents the design and implementation of a high resolution objective lens for imaging ultracold atomic clouds of sodium and lithium in the NaLi experiment. The lens has been developed using the ray tracing software OSLO. The design process aimed for an objective lens that performs diffraction limited at a high numerical aperture of 0.41 for both imaging wavelengths of sodium (589nm) and lithium (671nm). Additionally, the lens design accounts for the requirements regarding the installation into the existing experiment, determining the diameter and working distance of the imaging objective.

A tolerancing analysis was performed on the final lens design to assess the feasibility of production and mounting of the lens assembly by a suitable manufacturer. As for the implementation into the setup a versatile mechanical mount system has been built that provides mounting for the objective lens as well as the secondary optics contained in the imaging setup. Compounded with a translational and tilting stage the mount offers the necessary degrees of freedom for alignment of the imaging path.

Measurements in a test setup rendered a resolution close to the diffraction limit for a numerical aperture of 0.35 which is in good agreement with the tolerancing analysis.

## Zusammenfassung

Diese Arbeit beschreibt die Entwicklung und Umsetzung eines hochauflösenden Objektivs für die Bildgebung von ultrakalten Atomwolken aus Natrium und Lithium für das NaLi Experiment. Das Objektiv wurde mit der Raytrace Software OSLO entwickelt. Die Vorgaben während der Entwicklung waren, dass das Objektiv beugungsbegrenzte Bildgebung bei hoher numerischer Apertur (0.41) für beide Wellenlängen von Natrium (589nm) und Lithium (671nm) ermöglicht. Darüber hinaus wurde darauf geachtet, dass notwendige Kriterien für den Einbau in das Experiment eingehalten werden, dazu zählen der Arbeitsabstand und der Außendurchmesser des Objektivs.

Um die Umsetzbarkeit des Objektivdesigns durch einen Hersteller abzuwägen, wurde eine Toleranzanalyse durchgeführt. Für den Einbau des Objektivs mit allen zusätzlichen optischen Elementen in das Experiment wurde eine mechanische Vorrichtung gebaut, die zusätzlich mit einer Ausrichtungsmechanik ausgestattet ist, welche es ermöglicht die Apparatur in allen nötigen Freiheitsgraden zu bewegen um die Bildgebung auszurichten.

Messungen in einem Testaufbau ergaben, dass das Objektiv eine Auflösung nahe am Beugungslimit für eine numerische Apertur von 0.35 aufweist. Dies ist in guter Übereinstimmung mit der durchgeführten Toleranzanalyse.



# Contents

<b>1. Introduction</b>	<b>9</b>
<b>2. Image Formation</b>	<b>11</b>
2.1. Diffraction Integral	11
2.2. Diffraction by a Lens	13
2.3. Coherent Image Formation	15
2.4. Resolution	17
2.5. Aberrations	19
<b>3. Lens Design</b>	<b>21</b>
3.1. Initial Considerations	21
3.2. Optimizing the Lens Design using OSLO	24
3.2.1. Properties of the Final NaLi Lens Design	26
3.2.2. Simulated Imaging Performance of the NaLi Objective Lens	27
3.3. Tolerancing	30
3.4. Mounting	33
<b>4. Characterization of the Imaging System</b>	<b>37</b>
4.1. Test Setup	37
4.2. Image Analysis	39
4.2.1. Magnification	41
4.2.2. PSF analysis	41
4.2.3. Determining the Best Focus	42
4.2.4. Depth of Field (DOF)	45
4.2.5. Resolution	46
4.2.6. Field of View (FOV)	47
4.3. Conclusion on Tested and Designed Properties	48
<b>5. Conclusion and Outlook</b>	<b>51</b>
<b>A. Appendix</b>	<b>53</b>
<b>List of Figures</b>	<b>55</b>
<b>List of Tables</b>	<b>57</b>
<b>Bibliography</b>	<b>59</b>



# 1. Introduction

Optical image formation is of utmost importance for humankind as the sense of vision is the predominant tool we use to perceive our environment, especially considering that the processing of vision takes up more resources in the human brain than the four other senses together [30]. The human eye is yet not the only optical device we are using. The desire to explore domains that are otherwise hidden from the unaided eye stimulated the development of many other optical devices like cameras, telescopes, microscopes, eyeglasses or binoculars, which are ever-present in science and everyday life.

Today, image processing is an exciting multidisciplinary scientific field of its own. Moreover it provides many crucial techniques for other research areas. Among them is also the field of ultracold quantum gases. Since the first observation of Bose-Einstein condensation of atoms (BEC) in 1995 [2], [8] this field has immensely grown. Cold quantum gases proved to be a versatile test system for many fundamental concepts of quantum mechanics like the observation of matterwave interference [3], the Mott insulator transition [16] or the BEC-BCS crossover [14], [23] just to name a few examples.

Most quantum gas experiments have in common that diagnostics and data acquisition is done by means of optical imaging. For observing BECs two main techniques are used: In-situ and time of flight imaging. In both cases the interaction between atoms and light is used to obtain an image representing the density distribution of the atoms [25]. Generally one can distinguish between destructive and non-destructive imaging techniques. A common destructive imaging technique is absorption imaging [37], [31]. Here the atomic cloud is illuminated with a resonant laser beam and the shadow on the beam due to absorbed photons is detected on a CCD camera. Each absorbed photon transfers roughly one unit of recoil energy to the atomic cloud and causes a significant amount of heating, which generally limits this technique to only one “snapshot” per realized cloud.

Fluorescence imaging is a technique that, similar to absorption imaging, is based on scattering photons off atoms. In this case, however, one does not detect the “missing” photons in the laser beam but collects directly the scattered photons. The amount of signal in fluorescence imaging is significantly lower than in absorption imaging since only a small fraction of scattered photons can be captured by the imaging system. However, a big advantage of fluorescence imaging is the low background in the images that has been used to develop spatially resolved single atom detection in optical lattices [5],[42],[35].

Non destructive imaging techniques utilize the effects that atoms exert on off-resonant light. This can be for instance a phase shift (phase contrast imaging [4]) or polarization rotation (Faraday imaging [10]) of the imaging light.

All these techniques share the same technical aspect that the image is formed by means of optics (mirrors, lenses, imaging objectives) which makes optical devices a crucial part of each experiment. Recent progress in cold quantum gases experiments (atoms in optical lattices, single

## 1. Introduction

atom detection) have imposed high requirements on imaging objectives. The in situ imaging of atoms loaded into optical lattices requires a high spatial resolution of the imaging system as typical lattice spacings are in the range of one micrometer and below. Towards spatially resolved single atom detection one has to ensure that the imaging system covers a large solid angle of the scattered photons to overcome the otherwise low count rate.

Previous work done in our group (NaLi experiment) included the creation of ultracold Bose Fermi mixtures of sodium and lithium to study the interactions between a quantum mechanical system and its environment. For this purpose lithium ( ${}^6\text{Li}$ ) atoms were loaded into an optical lattice and immersed into a bath of a sodium ( ${}^{23}\text{Na}$ ) BEC. This system was used to investigate the motional coherence of the lithium atoms [40] as well as to observe the phononic lamb shift with a synthetic vacuum [38]. The measurements in these experiments were based on a band mapping technique [15], including absorption images taken after time of flight. The demands on the imaging optics in that case have not been too strict, therefore an already available microscope objective has been used that was originally designed for stereomicroscopy (Carl Zeiss SV 6/11). An estimation of the resolution of the imaging system including that imaging objective yielded roughly  $5\mu\text{m}$ .

Future projects for the NaLi experiment will evolve around a quantum simulator for problems related to quantum electrodynamics (QED) and dynamic gauge fields, with a proposed system described in [24] (Schwinger pair production). For these kind of experiments high resolution in situ imaging of atoms loaded into optical lattices is highly desirable. Therefore the implementation of a new imaging system featuring a high resolution imaging objective that is designed for the specific demands of the experiment has been undertaken, which is the subject of this work. The thesis is structured in the following way:

- Chapter 2 outlines the basic theory of image formation by lenses. Focus is put on defining the important parameters and relations that are used throughout the rest of the thesis.
- Chapter 3 describes the comprehensive process of lens design. This includes an initial draft of ideas and requirements, the simulation and optimization of lens design using the software OSLO, a tolerancing procedure that evaluates the lens design regarding technical realizability and the design of a mounting and alignment solution for the imaging lens and other optical components.
- Chapter 4 is dedicated to the experimental evaluation of the manufactured new imaging objective in a test setup. The important imaging properties are determined and compared to results of the simulations. Moreover the technical aspects of the mounting stage are summarized.
- Chapter 5 shows the first experimental results of the new imaging system installed in the real experiment and an outlook is given for future steps to improve the imaging and analysis process.

## 2. Image Formation

This chapter provides a theoretical background for the effects and properties associated with lens based optical imaging that will aid in understanding the lens design and analysis procedures used in this thesis. Important relations and definitions like resolution or numerical aperture that will be frequently used throughout the following work will be derived and discussed.

The chapter will be structured as follows: In the beginning the concept of diffraction is introduced as a necessary extension to geometric optics and the diffraction integral in Fresnel approximation is described in more detail. Afterwards the diffraction theory is applied to a spherical lens and the concept of diffraction limit is explained. In the next step the theory of coherent image formation is formulated by joining all previous findings. Particularly the relation between object and image described by a convolution is pointed out. Finally imaging aberrations and their inclusion into diffraction theory are shortly mentioned. For the sake of simplicity compact formulation is chosen over mathematically rigorous entirety in this chapter. The derivations will mostly follow the ones given in [18], in addition also [7],[19] or [28] are recommended for a comprehensive treatment of the scientific field of optics.

### 2.1. Diffraction Integral

In the scope of geometrical optics light is described by rays travelling in straight directions when propagating through a homogeneous medium. These rays represent the direction of energy flux of the light. The sketch in Figure 2.1 shows the occurrence of image formation in terms of geometrical optics by means of a positive lens. It is the property of an optical system to make a

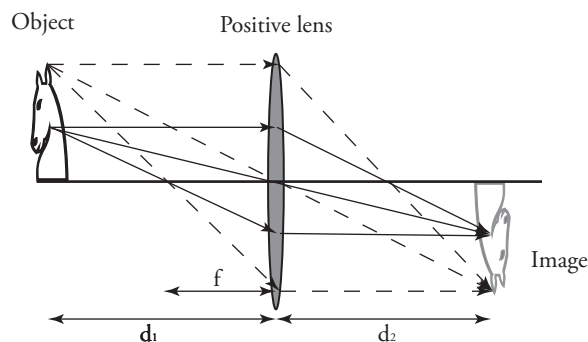


Figure 2.1.: Sketch of geometrical image formation by means of a positive lens. The lines represent light rays emanating from certain points of the object. The horse has to be considered perspectively extending into the paper plane. The image formed by a positive lens is upside down and mirrored. Here the magnification is unity.

## 2. Image Formation

part of light rays that are emitted from one point of an object on one side of the optical system converge into a point on the other side. The sum of these points comprises the image, which resembles the spatial light distribution of the object at another position in space. In the case of the optical system being a thin lens image formation occurs when the lens equation is met:

$$\frac{1}{d_1} + \frac{1}{d_2} = \frac{1}{f} \quad (2.1)$$

Here  $d_1$  is the distance between object plane and lens,  $d_2$  is the distance between lens and image plane and  $f$  is the focal length of the lens. In this description a point light source in object plane produces a point image in image plane. In practical use however this is not the case and the image of a point source has always a finite spatial extent. This circumstance is called the diffraction limit, as diffraction is the effect causing a lower bound for the spatial spread of a point source's image.

Diffraction is a phenomenon occurring when propagating waves (and in that regard light, too) are obstructed by an obstacle. A characteristic of diffraction is the appearance of dark and bright fringes in the vicinity of the obstacle's boundaries. In general the effects of diffraction are more dominant when the structure size of the obstruction is on the order of the wavelength at consideration.

Mathematically the effects of diffraction can be described by the Fresnel diffraction integral:

$$U_2(x_2, y_2) = \frac{i \exp(-ik\lambda)}{\lambda z} \iint_{-\infty}^{\infty} U_1(x_1, y_1) \exp \left\{ -\frac{ik}{2z} [(x_2 - x_1)^2 + (y_2 - y_1)^2] \right\} dx_1 dy_1 \quad (2.2)$$

With the notation used according to the coordinate system shown in [Figure 2.2](#).  $U_2(x_2, y_2)$

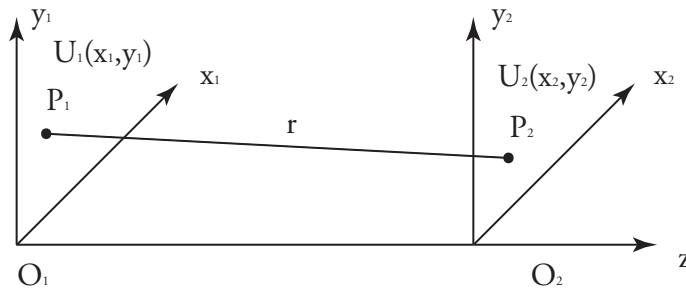


Figure 2.2.: Notations and coordinate system used for [Equation 2.2](#). The subscript 1 represents the diffraction plane, subscript 2 the observation plane.

describes the complex light field in the observation plane,  $U_1(x_1, y_1)$  is the complex field in the diffraction plane,  $i$  is the imaginary unit,  $\lambda$  the light's wavelength. The Fresnel diffraction integral is valid for the case that the observation point  $P_2$  is not far away from the optical axis, i.e.  $(x_2 - x_1)^2 + (y_2 - y_1)^2 \ll z^2$  (paraxial approximation). The integral describes the light field as a superposition of spherical waves emanating in the  $(x_1, y_1)$  plane and propagating along the  $z$  direction.

## 2.2. Diffraction by a Lens

We now shall apply the formalism of the Fresnel diffraction integral to light impinging on a lens. We choose the textbook example of a thin positive lens with spherical surfaces. A plane wave  $U_0$  is incident upon this lens and the light distribution in the focal plane at  $z = f$  is considered, see [Figure 2.3](#). Right before the lens the field is  $U_1(x_1, y_1) = U_0$ . The lens

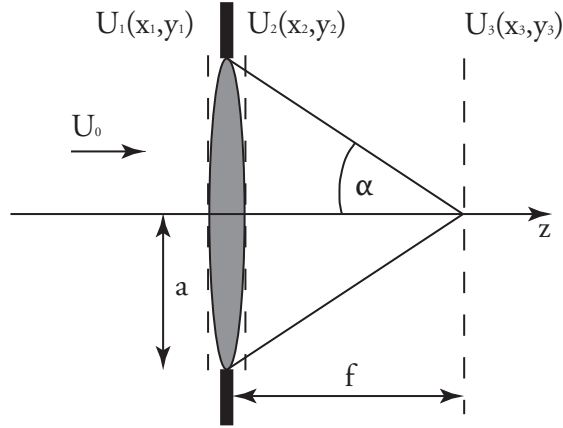


Figure 2.3.: Sketch of a lens.  $U$  represents the complex light field at different planes along  $z$  as described in the text,  $f$  is the focal length,  $a$  is the half diameter of the lens' clear aperture and  $\alpha$  describes the largest possible angle of the light cone formed by the clear aperture of the lens.

modulates amplitude and phase of the incoming field according to the complex transmittance  $t(x, y) = P(x, y) \exp \left[ \frac{ik(x^2 + y^2)}{2f} \right]$ .  $P(x, y)$  is called the pupil function of the lens and is confined by the clear aperture of the lens. The quadratic phase factor describes for positive  $f$  the convergence of an incident plane wave into the focus in terms of geometrical optics. Therefore the field right after passing the lens reads:

$$U_2(x_2, y_2) = U_0 P(x_2, y_2) \exp \left[ \frac{ik(x_2^2 + y_2^2)}{2f} \right] \quad (2.3)$$

The light field in the geometrical focal plane can now be determined by substituting [Equation 2.3](#) into the Fresnel integral [Equation 2.2](#) and choosing the plane of observation to be at  $z = f$ . In that case the quadratic phase terms of the Fresnel integral and the ones of the lens transmittance cancel out and it follows:

$$U_3(x_3, y_3) = \frac{iU_0}{\lambda f} \exp(-ikf) \exp \left[ -\frac{ik}{2f}(x_3^2 + y_3^2) \right] \int \int_{-\infty}^{\infty} P(x_2, y_2) \exp \left[ \frac{ik}{f}(x_3 x_2 + y_3 y_2) \right] dx_2 dy_2 \quad (2.4)$$

By defining the spatial frequencies  $m = x_3/f\lambda$  and  $n = y_3/f\lambda$ , the integral in [Equation 2.4](#) can be interpreted as the two dimensional Fourier transform of the pupil function  $P(x, y)$  at

## 2. Image Formation

spatial frequencies  $m$  and  $n$ . Most lenses are usually circularly symmetric. Therefore by using polar coordinates ( $r = \sqrt{x^2 + y^2}$ ) the pupil function of a lens with a clear aperture radius  $a$  can be written as:

$$P(r) = \begin{cases} 1, & \text{if } r \leq a \\ 0, & \text{otherwise.} \end{cases} \quad (2.5)$$

In this case Equation 2.4 can be analytically solved, yielding

$$U_3(r_3) = \frac{i\pi a^2}{\lambda f} \exp(-ikf) \exp\left(-\frac{i\pi r_3^2}{\lambda f}\right) \left[ \frac{2J_1\left(\frac{2\pi r_3 a}{\lambda f}\right)}{\left(\frac{2\pi r_3 a}{\lambda f}\right)} \right], \quad (2.6)$$

where  $J_1$  is the Bessel function of the first kind. We now introduce the numerical aperture NA of a lens as

$$\text{NA} = n \sin \alpha \approx n \frac{a}{f}, \quad (2.7)$$

with  $n$  being the refractive index of the surrounding medium of the lens (generally air or sometimes immersion oil in case of an object slide of a microscope). As seen in Figure 2.3 the NA is a measure for the opening angle of the cone of light that is formed by the outermost free aperture of the lens. The intensity distribution in the focal plane is determined by the modulus square of the complex light field. Performing this and using the definition of NA for a lens in air ( $n \approx 1$ ) the intensity in the focal plane reads

$$I(r_3) = \left(\frac{\pi^2 a^2}{\lambda z}\right)^2 \left[ \frac{2J_1\left(\frac{2\pi r_3 \text{NA}}{\lambda}\right)}{\left(\frac{2\pi r_3 \text{NA}}{\lambda}\right)} \right]^2. \quad (2.8)$$

This function is called Airy disc and its functional behaviour is shown in Figure 2.4. The Airy

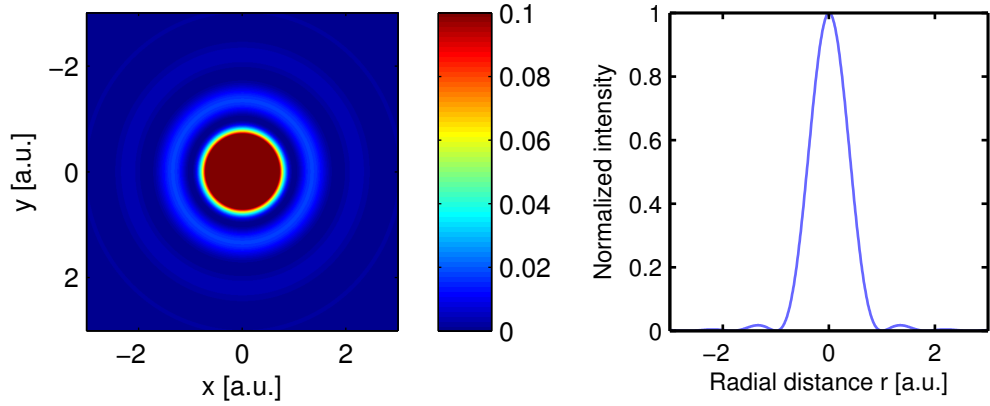


Figure 2.4.: **Left:** Airy disc as a false color image normalized to one. In order to make the side maxima visible the coloraxis is chosen 10% of the peak value, overexposing the central peak. **Right:** One dimensional profile through the maximum of the Airy disc.

disc is a radial symmetric function with a central bright spot that contains about 80% of the intensity. The central maximum is surrounded by fringes with decreasing amplitude (1st side maximum is 1.75% of the central peak). The radial distance between the center peak and the first dark ring of the pattern is usually used to estimate the extent of the central bright spot. The first minimum of the Airy pattern occurs when the argument in Equation 2.8 takes the value of about  $1.22\pi$ . From that follows that the first dark ring appears at a distance

$$r = \frac{1.22\lambda}{2\text{NA}} \quad (2.9)$$

from the pattern's center. This relation shows that a lens can focus light only into a patch of finite size, which is inversely proportional to the NA. This fact is commonly referred to as the diffraction limit as it is a fundamental limit imposed by the wave nature of light, even in the absence of any experimental imperfection.

### 2.3. Coherent Image Formation

In the previous section the effects of diffraction were studied for the case of an incoming collimated beam being focused by a lens. It was shown that in contrast to geometrical optics, that predict a point like intensity distribution, the intensity pattern in the focal plane has a specific shape with radial extent inversely proportional to the lens' NA.

In this section the effects of diffraction on a lens' imaging performance are examined. We consider the case of a thin object placed in the  $(x_1, y_1)$ -plane in front of a thin lens situated in the  $(x_2, y_2)$ -plane and imaged on the  $(x_3, y_3)$ -plane, see Figure 2.5. The object is illuminated with a plane wave of unity amplitude, thus the field right after the object is  $U_1(x_1, y_1) = o(x_1, y_1)$ , with  $o(x_1, y_1)$  being the amplitude transmittance of the object. The derivation of the complex field in the plane of observation follows the same construction as in the previous section: The function  $o(x_1, y_1)$  is propagated for the distance  $d_1$  by means of the Fresnel integral to the plane right before the lens, then it is multiplied by the lens transmittance according to Equation 2.3 and afterwards it is "diffraction propagated" the distance  $d_2$  to the observation plane. This procedure renders the lengthy result

$$U_3(r_3) = \frac{M \exp[-ikd_1(1 + 1/M)]}{d_1^2 \lambda^2} \exp \left[ -\frac{ikM}{2d_1}(x_3^2 + y_3^2) \right] \int \int_{-\infty}^{\infty} o(x_1, y_1) \exp \left[ -\frac{ik}{2d_1}(x_1^2 + y_1^2) \right] h(x_1 + Mx_3, y_1 + My_3) dx_1 dy_1, \quad (2.10)$$

where  $M$  is defined as  $M = d_1/d_2$ , and the function  $h(x, y)$  is defined as

$$h(x, y) = \int \int_{-\infty}^{\infty} P(x_2, y_2) \exp \left[ -\frac{ik}{d_1}(x_2x + y_2y) \right] dx_2 dy_2, \quad (2.11)$$

which is the two dimensional Fourier transform of the pupil function  $P(x_2, y_2)$ . The function  $h(x, y)$  is of great importance for the description of the imaging process. Consider the case

## 2. Image Formation

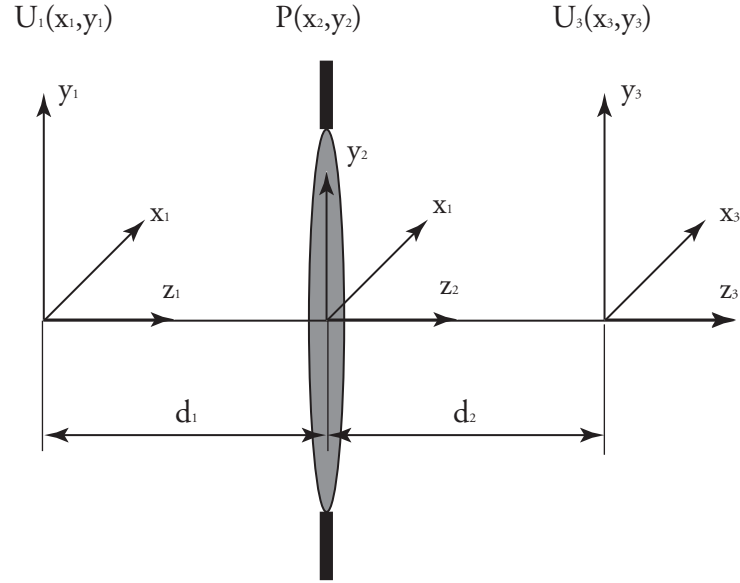


Figure 2.5.: Notations and coordinate system used for the formulas of image formation. The distance between object (image) plane and lens is denoted by  $d_1$  ( $d_2$ ) and they fulfill the lens equation [Equation 2.1](#).

where the object represents a point like light source, then the object transmittance can be expressed by delta functions

$$o(x_1, y_1) = \delta(x_1)\delta(y_1). \quad (2.12)$$

Substituting this term into [Equation 2.10](#) one derives an expression for the image of a point like object

$$U_3(r_3) = \frac{M \exp[-ikd_1(1 + 1/M)]}{d_1^2 \lambda^2} \exp \left[ -\frac{ikM}{2d_1}(x_3^2 + y_3^2) \right] h(Mx_3, My_3), \quad (2.13)$$

which is besides phase factors represented by the function  $h(x, y)$  as defined in [Equation 2.11](#).  $h(x, y)$  is therefore called the amplitude point spread function (APSF) of the imaging system as it describes how the image is an altered version of the point object (which is in general a spread). Comparing the definition of  $h(x, y)$  with the integral part of [Equation 2.4](#) yields that, besides a different value in the denominator of the phase factor, the integral is the same. Thus the spread of the image of a point like object is quantitatively described by an Airy disc as well. As a next step the image of an extended object is considered. Knowing that  $h(x, y)$  is representing the image of a point source we can assume that for a good imaging system  $h(x, y)$  behaves functionally the same as the object in a sense that it has a sharp peak and falls off rapidly outside the region where the argument  $x$  or  $y$  in  $h(x, y)$  is zero. Therefore we can use the approximation  $x_1 \approx -Mx_3$  and  $y_1 \approx -My_3$  in [Equation 2.10](#) to take the phase term out of

the integral part of the equation, which when simplifies to

$$U_3(r_3) = \frac{M \exp[-ikd_1(1 + 1/M)]}{d_1^2 \lambda^2} \exp \left[ -\frac{ikM}{2d_1} (x_3^2 + y_3^2)(1 + M) \right] \iint_{-\infty}^{\infty} o(x_1, y_1) h(x_1 + Mx_3, y_1 + My_3) dx_1 dy_1, \quad (2.14)$$

and in terms of intensity it yields

$$I_3(r_3) = \left( \frac{M}{d_1^2 \lambda^2} \right)^2 \left| \iint_{-\infty}^{\infty} o(x_1, y_1) h(x_1 + Mx_3, y_1 + My_3) dx_1 dy_1 \right|^2. \quad (2.15)$$

The integral term in both equations can mathematically be interpreted as a two dimensional convolution. Hence the image of a thin object can be evaluated by convolving object transmittance and spread function of the imaging system.

At this point it is important to note that so far a coherent imaging process was considered. As a result the formulas derived treat the evolution of the complex light field first and in the last step the modulus square is taken to get an expression for the intensity distribution. Without derivation we give the equivalent result to [Equation 2.15](#) for the case of incoherent imaging:

$$I_3(r_3) = \iint_{-\infty}^{\infty} I_0(x_1, y_1) |h(x_1 + Mx_3, y_1 + My_3)|^2 dx_1 dy_1, \quad (2.16)$$

where  $I_0(x_1, y_1)$  is the intensity distribution in the object plane,  $|h(x, y)|^2$  is called the intensity point spread function (IPSF). Since this is the function of interest for the rest of this thesis we shall refer to it as the PSF. The main difference between coherent and incoherent image formation in this formalism is the succession of convolution and taking the modulus square. For the object being approximately a point source both [Equation 2.16](#) and [Equation 2.15](#) produce the same result. This is of particular importance in [chapter 4](#), where the PSF of an imaging objective has been measured by imaging a small pinhole.

## 2.4. Resolution

Having laid the foundation for the description of the imaging process by a lens, we now define the property of spatial resolution that is of particular importance for the application of atom imaging concerned in this thesis. Resolution is a widely used and important concept in natural sciences, however, different ambiguous definitions exist. In this section we shall elaborate on the traditionally used definition known as the Rayleigh criterion of resolution that has an intuitive description based on the human eye's capability to distinguish structures, [\[36\]\[17\]](#).

Consider an object comprised of two points that is incoherently imaged. The case of two points is not just a generic example but has a physical meaning in the field of astronomy (where many early studies on optics have been performed). The observation of two closely neighbouring stars with a telescope represents in good approximation two incoherent point like light sources. The image of two point like objects is according to [Equation 2.16](#) two individual PSFs centered around the geometrical image positions of the point objects. Assuming an incoherent imaging process

## 2. Image Formation

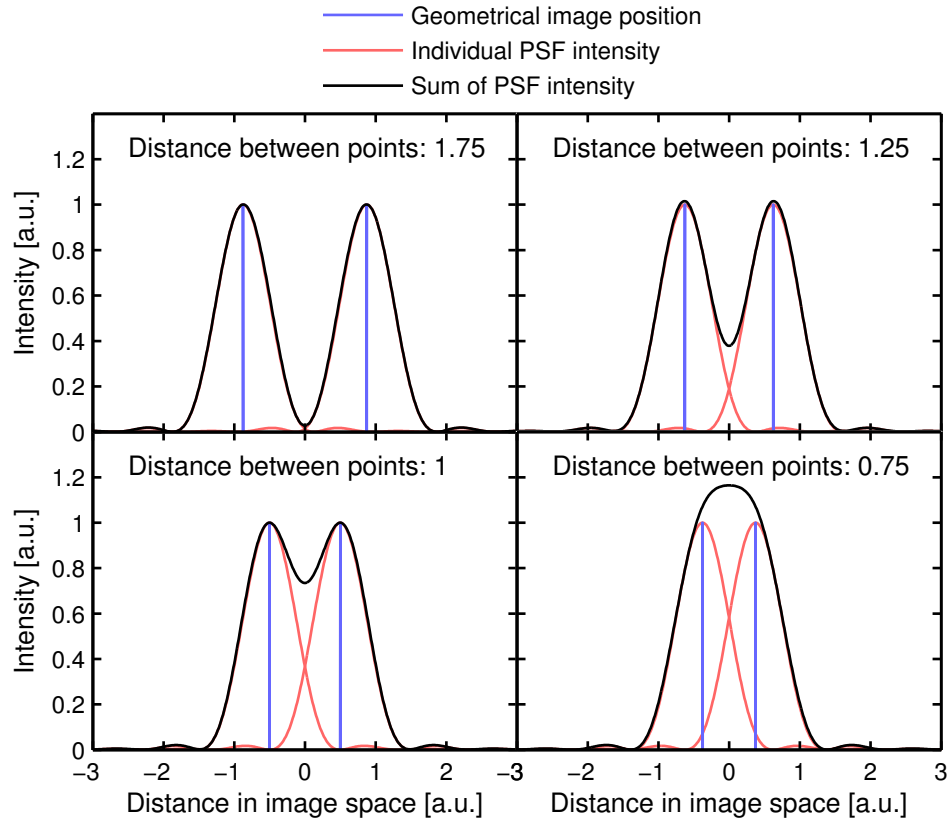


Figure 2.6.: Graphical illustrations of Rayleigh's criterion. The incoherent images of two point sources are shown for varying point separation. The PSFs in this example are Airy discs with the first minimum appearing at 1 [a.u.]. The case of Rayleigh's criterion is depicted in the lower right image. Here the distance of the geometrical image points coincides with the position of the first dark ring of the Airy disc. The resulting intensity distribution implies to separable peaks.

the resulting intensity distribution in image space is the sum of the PSFs. This is illustrated in [Figure 2.6](#). The PSFs overlap depending on the distance between the object points. The distance where two points can yet be distinguished in the image is referred to as the resolution. The point marking the transition between distinguishability and not is to a certain degree a subjective issue. The criterion of resolution proposed by Rayleigh is when the maximum of one PSF falls on the position of the first minimum of the other (bottom left in [Figure 2.6](#)). In that case the intensity in the middle dip of the intensity pattern amounts to about 73%. For optical systems whose PSFs are described by Airy discs the resolution is then given by [Equation 2.9](#) as the position of the first dark ring

$$r = \frac{1.22\lambda}{2NA}. \quad (2.17)$$

This expression has already been encountered in the case of a homogeneous collimated beam that is focused by a lens. In both cases diffraction is the limiting factor for the finite size of both, the focus spot and the resolvable structure in an image.

Note that for the case of coherent or partially coherent imaging defining resolution is more involved. In that case, [Equation 2.15](#) has to be used where first the overlap of the complex field has to be evaluated which in return depends on the phase relation of both point like light sources. It was shown in [7], however, that the resolution for coherent and incoherent illumination follows, apart from a different numerical value (larger for coherent illumination), the same relation  $r \propto \lambda/\text{NA}$  i.e. it is essentially determined by the NA of the imaging system. The Rayleigh criterion has been used in the course of this thesis as it is a reasonable measure for the resolving properties of an imaging objective which has been the main object of investigation in this work.

In recent years a lot of effort has been put into imaging techniques that are not limited by the diffraction limit. These so called superresolution techniques make use of effects including dark states or photon counting statistics. As these techniques are beyond the framework of this thesis the interested reader is referred to the work of e.g. [44][20][47][22].

## 2.5. Aberrations

The theoretical framework up until now has been developed disregarding the errors that occur in every real imaging system. These imaging errors are called aberrations and they represent deviations in the theoretically predicted image formation. More formally aberrations can be described as wavefront deviations. In a perfect imaging system that is free of aberrations the wavefront at the exit aperture is a sphere converging towards the geometrical image point. Aberrations cause the real wavefront to deviate from this spherical shape, see [Figure 2.7](#). This difference between spherical and real wavefront is referred to as the optical path difference (OPD) given in units of wavelengths. Aberrations in a lens can be caused by different effects including not fulfilling the paraxial approximation, misalignment, tilt or physical imperfections of the lens. Aberrations are a well studied subject in optics, therefore a detailed description of origin and appearance of typical aberrations is omitted here. For a detailed mathematical description of the topic the reader is referred to [7] or the original work by Zernike [9].

One main goal of this work has been to create a new imaging objective for atom imaging that features a high resolution on the order of one micrometer. The definition of resolution previously made suggests that in order to increase resolution for a given wavelength one has to increase the NA of the system. However, going to high NA implies imaging beyond the paraxial approximation which can cause a detrimental loss of image quality when the optical system is not corrected for aberrations. This is the goal of lens design. The aberrations that are present in single lenses can be cancelled out to a certain degree by an appropriate arrangement of multiple lenses. Camera and microscope objectives are therefore comprised of a sophisticated assembly of lenses to correct for specific aberrations [26].

The goal of the lens design procedure described in [chapter 3](#) is to come up with an imaging objective design that works with a high NA while reducing aberrations as good as possible. The lens design has been performed by means of a computational software that can simulate

## 2. Image Formation

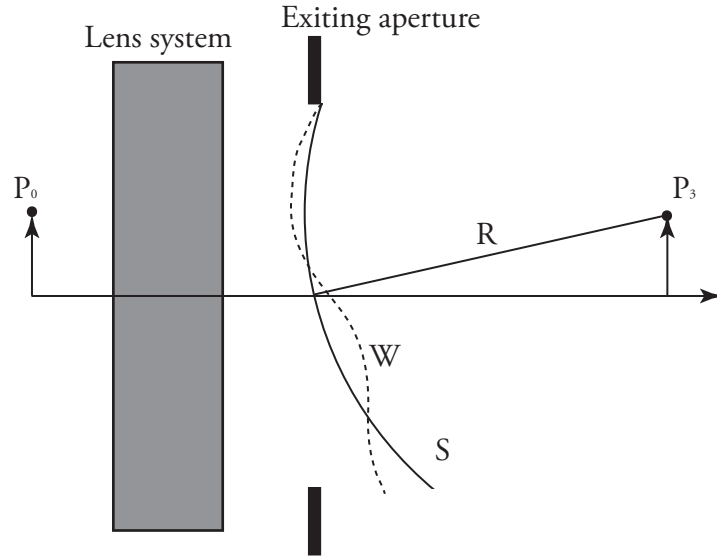


Figure 2.7.: Sketch illustrating aberrations in a diffraction description. The point  $P_0$  is imaged as  $P_3$ . The wavefront of light at the exit aperture of an (theoretical) aberration free system has a spherical surface  $S_s$ . Due to aberrations the wavefront  $W$  deviates from  $S$ .  $R$  is the radius of the sphere  $S$  converging towards the point  $P_3$ .

the properties of an imaging system including an analysis of the PSF and the wavefront error. Therefore it is important to have a quantitative measure for the image quality of the lens system i.e. a figure of merit for the amount of aberrations that can be tolerated in a system. A reasonable condition is given by Maréchal [29]. He states that an image forming system can be considered well corrected when the root-mean-square (rms) wavefront deviation  $OPD_{rms}$  is not larger than  $1/14$  ( $\approx 0.07$ ) of a wavelength. In this case the so called Strehl ratio is still 0.8 or higher. The Strehl ratio is defined as the ratio of the peak intensity in the diffraction pattern of a system exhibiting aberrations and the PSF of a perfect system

$$S = \frac{I_{aberrations}}{I_{perfect}}, \quad (2.18)$$

and is a descriptive measure for image quality (note that the position where the intensity pattern of the aberrated system exhibits its peak value does not necessary coincide with the peak value position of the unaberrated PSF). In the presence of small aberrations  $OPD_{rms} < 0.07$  the PSF has a decreased peak value yet the functional shape is still resembling the one of an unaberrated system. The missing intensity at the peak position is redistributed outwards. For more dominant aberrations the distortion of the PSF from an airy disc is way harder, compare the simulations in subsection 3.2.1, not only is the peak value reduced, but the PSF can exhibit multiple peak structures, asymmetries and a general spread of the function outwards.

These two criteria ( $OPD_{rms} < 0.07$  and  $S > 0.8$  respectively) have been applied in the lens design procedure in the following chapter as these values can conveniently be evaluated with numerical methods.

## 3. Lens Design

This chapter summarizes the process of lens design. It starts with general considerations about the purpose of the imaging objective in the experiment, which properties it should fulfill and what restrictions might be imposed on it. Next step is the simulation of a possible lens design with OSLO (Optics Software for Layout and Optimization). Here, different combinations of lenses are iteratively altered and checked for best performance. Of great importance in this step is a suitably chosen measure of performance that is evaluated in the simulations, therefore it should reflect accurately the desired demands on the lens. After finding an optimum lens design in the simulations a tolerancing analysis has to be performed. Tolerancing evaluates the performance of the lens design in terms of technical realizability. The purpose of the tolerancing analysis is to determine a lens design that is most stable against these variations in the manufacturing process. Finally, the technical issues of incorporating the lens into the imaging setup have to be evaluated. This includes mechanical mounting and the possibility of alignment of the imaging lens.

### 3.1. Initial Considerations

In the following the parameters that are important to consider in the beginning of the lens design are discussed. In this phase it is not about to come up with a final solution but rather to check that all requirements on the imaging objective are considered and to estimate the feasibility of these requirements.

- **Resolution:** The resolution of an imaging objective determines the size of details that can be extracted from the images. Thus the resolution should be at least the same size or smaller than the structure one wants to observe. Two lengthscales are of interest for the NaLi experiment: First, the healing length  $\xi$  [34] which describes the smallest scale where density modulations occur in BECs and which is on the order of a micrometer for typical trap parameters. Second, the site spacing of the optical lattices that we plan to employ in the experiment. For the proposed lattice setup the spacing is tunable in the range of a couple micrometers.
- **Depth of Focus (DOF):** The DOF of an imaging objective defines the range on the optical axis where an image spot is still considered focused. Usually defined as twice the distance from the smallest spot size to where the spot area is doubled [39]. Alignment procedure and alignment hardware has to be chosen according to the DOF of an objective as it determines the required precision with which the optics have to be positioned. As the DOF reduces quadratically as the resolution is reduced (see Rayleigh range [39]), the

### 3. Lens Design

requirements on the alignment can increase drastically. As shown in [31] a DOF of  $6.8\mu\text{m}$  is reasonable to perform absorption imaging with sufficient technical stability.

- **Field of View (FOV):** The field of view is the sector in the object plane that is reproduced in the imaging setup. It therefore depends on the magnification of the imaging setup as well as on the chip size of the CCD camera. As it will be described in subsection 3.2.1, the imaging objective will be used in an infinity corrected microscope setup in which the magnification can be conveniently changed and thus also the FOV can be adjusted. In this regard two limitations have to be considered: First, the magnification should not be chosen lower than the value where the extent of an airy disc fills one pixel of the CCD chip. If chosen lower, the resolution of the imaging system will not longer be determined by the imaging objective but will degrade due to the coarse grain of the image plane. Second, as the magnification is lowered and thus the FOV is increased, the limitation in view angle will not be due to the finite chip size of the CCD camera but due to the reduction in image quality caused by aberrations related to off axis imaging. For the applications in our experiment the area of good image quality should extend over the range of a couple of hundred micrometers.
- **Imaging Wavelengths:** Absorption imaging and fluorescence imaging, the most common imaging techniques in ultracold atom experiments, rely on resonant atom light interaction effects. Therefore imaging light is tuned close to resonance of the optical transitions of sodium ( $\lambda_{D2} = 589.158\text{nm}$  [43]) and lithium ( $\lambda_{D2} = 670.977\text{nm}$  [11]). The imaging objective has therefore to be well corrected for these wavelengths. In the beginning of this thesis it was considered to expand the NaLi mixture experiment and include bosonic potassium. Consequently the imaging objective should preferably be well corrected also for  $^{40}\text{K}$  ( $\lambda_{D2} = 766.701\text{nm}$  [45]). The objective has not only been designed for imaging but also for imprinting dipole potentials and lattices onto the atoms. For this purpose an infrared laser ( $\lambda = 1064\text{nm}$ ) and a green laser ( $\lambda = 532\text{nm}$ ) are available in the experiment. Therefore a wide range of wavelengths has to be taken into the optimization procedure to offer the desired versatility.
- **Geometrical Constrains:** Resolution and DOF depend on the NA of the imaging objective i.e. the spreading angle of the light cone emitted from the object that is collected by the objective. Therefore apart from any optical design the NA is limited by the smallest possible working distance and the largest possible diameter of the objective. The situation of space constrains in the NaLi experiment is shown in Figure 3.1. In close proximity of the vacuum cell the space in x direction is limited to 46mm by the cladding pair containing the coils for the magnetic trap. The location of the trapped atoms in the experiment is roughly centered in the middle of the vacuum cell. Therefore the estimated distance between the position of the atoms and the outer surface of the vacuum cell is 20mm which is the least possible working distance of an objective due to mechanical constrains (an exception is a lens design that includes parts inside vacuum, which we didn't pursued). Additionally to these 20mm the objective has to be moved further away from the cell to avoid a clipping of the MOT beams. Besides these "hard" limits on the outer dimensions

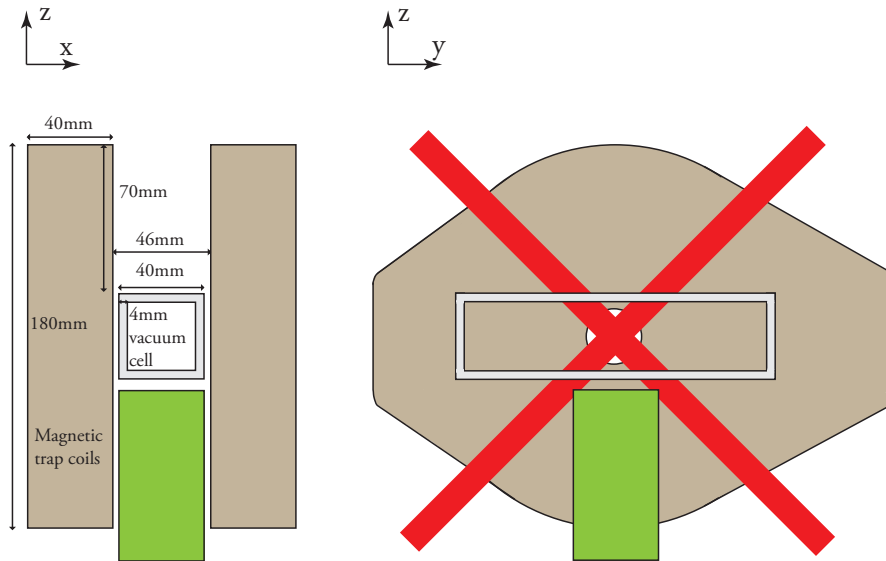


Figure 3.1.: Sketch of the vacuum cell and surrounding constructions of the NaLi experiment. Gravity as well as the imaging beam are pointing in  $-z$  direction. The atoms are propagating out of the oven in  $y$  direction. **Left:** Showing the constrains on the imaging lens dimensions due to the cladding of the magnetic trap coils. The green area shows the housing of the final imaging lens. **Right:** Showing possible constrains due to MOT beams (one cladding not shown in sketch for better visibility). Therefore the MOT beams size has been reduced and the lens mounting was sloped at the edge close to the cell.

of the objective one has to include a couple of millimeters of “wobble space” to account for any experimental deviations from the ideal case and to have a clear range where the objective can be moved freely.

- **Degree of Complexity of the Lens Design:** The complexity of the lens design refers to the shape, material and the number of individual elements used in the lens system. Basically one has to come up with a compromise between the desired performance of the imaging objective and the degree of complexity one is willing to accept. For instance the lens design can be comprised of spherical lenses which are known to suffer from spherical aberrations when used outside the paraxial regime. Aspheric lenses on the other hand suppress spherical aberrations greatly, however, are more difficult to manufacture and will generally be more costly and time consuming to purchase compared to lenses with spherical surfaces.

A similar assessment has to be done with the total number of elements in the system. Additional elements in the lens design can address specific aberrations, but again, additional elements increase the overall cost of the system and make the centering and mounting of the assembly more challenging.

Summing up, the lens design we aimed for is an imaging objective with an NA of about 0.4

### 3. Lens Design

that performs diffraction limited for at least the optical wavelengths of sodium and lithium. Constructing a system with a given NA is not difficult as this is a mainly geometrical property. The main part of the optimization procedure is to find a configuration of parameters that reduces aberrations in order to be diffraction limited.

## 3.2. Optimizing the Lens Design using OSLO

OSLO is a software that provides various analysis and optimization tools for lens design. To determine the aberrations present in an optical system, OSLO traces a large number of rays through the optical system by means of exact trigonometrical equations. Therefore it also accounts for effects outside the paraxial approximation. These simulation can be used to determine the wavefront OPD as well as the PSF in the presence of aberrations. These properties were used to quantitatively assess the lens design.

Moreover OSLO features an optimization algorithm that iteratively finds the lens system with least aberrations within given bounds and for specified parameters. For the lens design I followed a strategy recommended in [26]. It is based on the following steps:

1. Set a performance criterion for the lens system and find a measurable property corresponding to that performance in the simulation.
2. Find an initial guess for a lens system that is promising for meeting the performance requirements.
3. Alter the systems parameters while monitoring the simulated performance change of the system. The alteration can be done manually or by means of an optimization algorithm provided by the ray trace software.

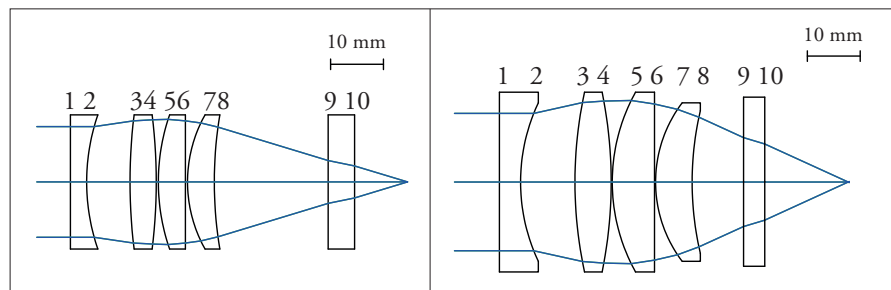


Figure 3.2.: Sketch of the lens system including collimated incoming beam (blue lines represent geometrical light rays). Lens design as described in [1] (**left**) that has been used as the initial guess with imaging wavelength  $\lambda = 852\text{nm}$  and the final lens design of this thesis after optimized for the requirements of the NaLi experiment (**right**) with imaging wavelength  $\lambda = 671\text{nm}$ . Surface 9 and 10 represent the wall of the vacuum cell, which has to be included into the optical optimization routine.

Based on the discussions mentioned in [section 3.1](#) we aimed to design an imaging objective with an NA of about 0.4 that performs diffraction limited for at least the optical wavelength

of sodium and lithium. As the quantitative criterion for diffraction limitation we assumed:  $OPD_{rms} \leq 0.07$  corresponding  $S \geq 0.8$ , see [section 2.5](#).

As an initial guess I first tried the lens design proposed in [33] or [32]. These, however, lacked the capability of performing at different wavelengths. More promising was a draft by W. Alt [1]. Here, a lens design is proposed that puts focus on cost efficiency while providing all essential imaging properties. This initial guess was the starting point that eventually led to the final NaLi design described in this thesis. [Figure 3.2](#) shows sketches of the W. Alt and NaLi design. Most prominent difference is that the NaLi design has increased lens diameter and reduced working distance thus increased NA. The optimization procedure is a combination of manual an

Surface	Radius of curvature [mm]	Distance to next surface [mm]	Surface diameter	Material
1	$\infty$	4.00	34.00	air
2	35.1	10.29	34.00	air
3	80.35	6.86	34.00	BK7
4	-80.35	0.20	34.00	air
5	35.00	8.00	34.00	BK7
6	$\infty$	0.20	34.00	air
7	24.89	6.91	30.00	BK7
8	59.16	9.74	30.00	air
9	$\infty$	4.00	32.00	fused silica
10	$\infty$	16.00	32.00	vacuum

Table 3.1.: Parameters of the lens components of the final lens design (rounded to two digits). The distance between surface 8 and 9 is subject to change for different wavelengths since the objective exhibits a chromatic focal shift as shown in [figure 3.3](#). The parameters shown below correspond to an imaging wavelength of  $\lambda = 671\text{nm}$ .

automated parameter alternation. OSLO features an optimization tool that performs a certain amount of iterations, in each changing the system's parameters (parameters that can be used as variables for the algorithm are the radius of curvature and the thickness of surfaces) in order to minimize a chosen error function (e.g. wavefront aberrations). This method's advantage compared to manual changes is that iterations are done much faster. However, the drawback is that while exploring the parameter space, the algorithm can converge towards a local minimum or can get stuck at bounds. Therefore the most reliable method turned out to be a sequential use of automated iterations followed by manual changes of bounds and surface parameters in order to enable the algorithm to explore further regions of the parameter space. Another technical detail worth mentioning here is that while using the algorithm one has to make sure to restrict the possible solutions to a given NA. What might happen is that the algorithm, in search for the least wavefront aberrations, will go to a low NA configuration (as these usual exhibit less aberrations) which is against the design goal of a high resolution lens system. This restriction can be done by setting proper bounds for the parameter changes or by predefining the convergence angle of the light beam from the last lens.

### 3.2.1. Properties of the Final NaLi Lens Design

The data of each lens of the NaLi imaging objective are summarized in [Table 3.1](#). The chosen lens design involves the following lens types (from left to right): Planoconcave lens, biconvex lens, planoconvex lens and meniscus lens. Surface 9 and 10 represent the wall of the vacuum cell (4mm thick, fused silica) which has to be included into the analysis as it is an element on the optical axis of the imaging path. The position of the atoms in this sketch corresponds to the focus (position of the three blue rays intersecting). For the sake of simplicity and cost efficiency the lens design is restricted to only spherical lenses out of BK7. In consultation with the manufacturer the diameter of the meniscus lens was reduced to avoid clipping of the MOT beams. Considering the free aperture of the lenses the imaging objective has a maximum NA of 0.41 and a working distance of 8.17mm (here, working distance is defined as the distance from the physical edge of the objective tube to the wall of the vacuum cell, see [Figure 3.4](#)).

Since no achromats are used in the design, the imaging objective exhibits a chromatic focal shift that is graphically shown in [Figure 3.3](#). The chromatic focal shift poses a problem when both

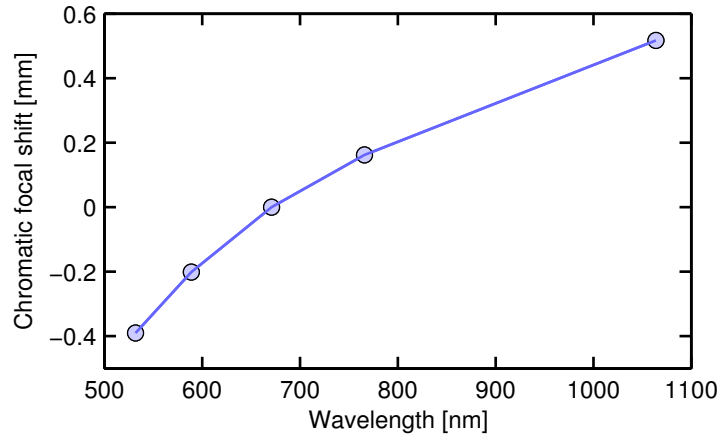


Figure 3.3.: Chromatic focal shift of the NaLi imaging objective. The shift is calculated relative to the lithium imaging wavelength ( $\lambda = 671\text{nm}$ ). The solid line is a guide to the eye.

species are imaged on the same camera, as one of the atomic clouds would be clearly out of focus. This is circumvented in our setup as we implemented the imaging objective in an infinity corrected microscope arrangement with dichroic mirrors to separate the imaging wavelengths onto two different cameras, see [Figure 3.4](#). In an infinity corrected system the specimen is placed right in the focal plane of the objective lens. Thus the collected light rays proceed parallel after the objective lens. Image formation is then enabled by means of a secondary lens, defining the image plane. The advantage of this system is that in the region between objective lens and secondary lens (region of parallel rays) further optical elements can be placed (filters, polarizers) without displacing the position of the image plane. Moreover the magnification  $M$  of the system doesn't depend on the relative position of the two lenses but only on the ratio of the focal lengths:

$$M = \frac{f_{\text{objective}}}{f_{\text{secondary}}} \quad (3.1)$$

Thus the magnification of the system can be conveniently changed by repacing the secondary lens and refocus of the camera, all without repositioning of the objective lens. The overall imaging path is designed such that the objective lens is placed in the focus of the sodium atoms, the residual chromatic focal shift of 0.201mm causes the light rays of the lithium light to diverge at an angle of 2.5mrad. This divergence can be taken care of by refocusing with the lithium camera. The refocus comes along with a deviation of the magnification from Equation 3.1 which has to be determined experimentally.

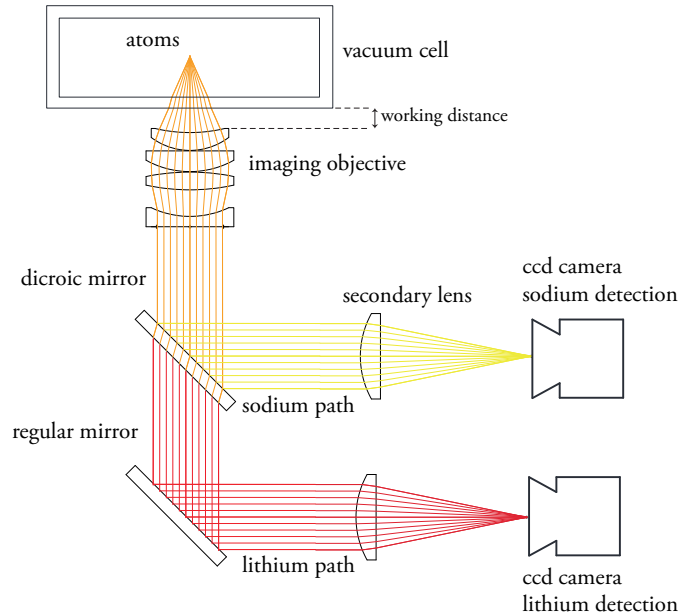


Figure 3.4.: Sketch of the infinity corrected microscopy setup as used in the NaLi experiment. The imaging objective is placed such that one species is in the focal plane (in this case sodium). The light is split in two different paths with a dichroic mirror and focused with secondary lenses onto separate cameras. Since lithium is not in the focus of the imaging objective the outgoing rays exhibit a slight divergence, that can be easily compensated by refocussing with the camera.

### 3.2.2. Simulated Imaging Performance of the NaLi Objective Lens

To evaluate the imaging properties of the objective lens, a configuration is simulated that takes into account the arrangement of an infinity corrected system. Therefore the maximal aperture of the objective is homogeneously illuminated with monochromatic light and the light distribution in the focus is analyzed. Note that the imaging process in the experiment has a reversed direction of propagation (from right to left in Figure 3.2) where the point-like irradiance of the atoms is collected by the imaging objective and collimated. For the evaluation of the imaging properties both processes are absolutely equivalent. Figure 3.5 left shows the intensity distribution of an on-axis point in the focal plane. The curves for different wavelengths are calculated for the focus of the individual wavelengths respectively. The peak values are

### 3. Lens Design

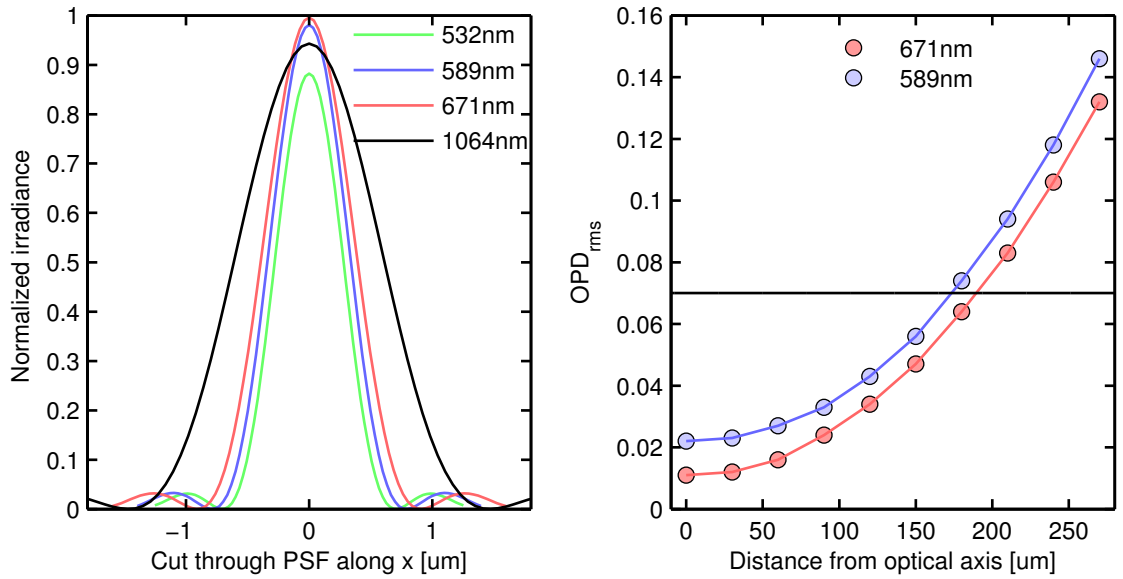


Figure 3.5.: **Left:** Profiles of the PSFs evaluated with OSLO for different wavelengths.

**Right:** Imaging performance in terms of  $OPD_{rms}$  for points away from the optical axis. The black line marks the value associated with the diffraction limit. From the graph the FOV reads as follows:  $FOV_{589nm} = 346\mu m$  and  $FOV_{671nm} = 380\mu m$ . The solid lines are guides to the eye.

all clearly above 0.8 indicating that the lens design is well corrected for on-axis points. The important imaging properties are summarized in Table 3.2 for the wavelengths of interest. As planned, the best performance is reached at the imaging wavelengths of lithium and sodium and slightly decreases towards the other sides of the spectrum. The shown PSFs are evaluated

Imaging wavelength [nm]	Diffraction limited resolution [ $\mu m$ ]	Strehl ratio S	Optical path difference $OPD_{rms}$	Depth of focus DOF [ $\mu m$ ]
532	0.78	0.87	0.055	5.5
589	0.87	0.98	0.022	6.5
671	0.99	0.99	0.011	7
1064	1.60	0.94	0.038	11

Table 3.2.: Relevant imaging properties of the lens design for the wavelengths of interest.

for a point on the optical axis. Due to the spatial extend of atomic clouds in the experiment ranging from tens to hundreds of micrometer, even if the atomic cloud is centered symmetrically on the optical axis, significant parts of it will suffer from off axis imaging aberrations. We define the FOV as twice the distance (in object space) from the optical axis to the point where

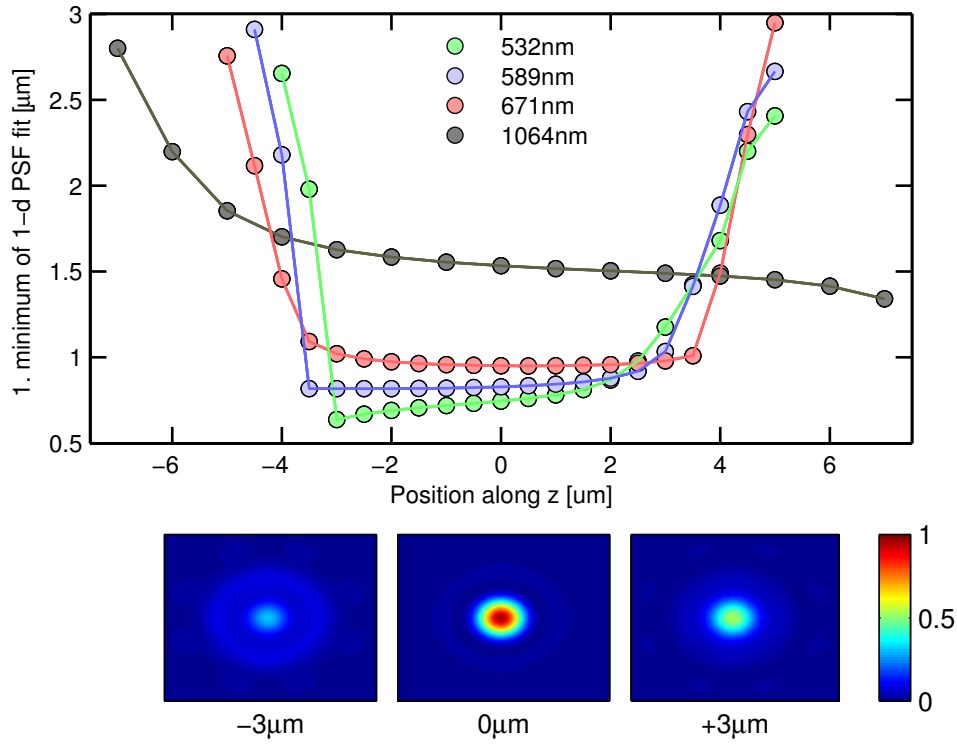


Figure 3.6.: Scan along the  $z$  axis through the point of best focus. To estimate the spot size of the intensity pattern a fit of the form Equation 3.2 was performed and the position of the 1. minimum ( $\Delta x$ ) was taken as a measure of the spread. At the bottom the raw pictures of the intensity pattern for 3 different positions (589nm) along  $z$  are shown. The picture size amounts to  $9.45\mu\text{m} \times 7.45\mu\text{m}$  in object space. Clearly an asymmetric behaviour can be seen. As DOF is defined the range where  $\Delta x$  is lower than  $\Delta x$  at the focus times  $\sqrt{2}$ . The solid lines are guides to the eye.

the diffraction limited imaging properties are lost ( $OPD_{rms} \geq 0.07$  corresponding  $S \leq 0.8$ ). Figure 3.5 right shows the  $OPD_{rms}$  as a function of distance from the optical axis. The FOV amounts to  $346\mu\text{m}$  for the 589nm wavelength and  $380\mu\text{m}$  for the 671nm wavelength. The DOF was determined by evaluating the intensity pattern around the focus in  $z$  direction. A one dimensional fit representing the profile of an Airy disc (see Equation 2.8) has been applied to the cut along the peak of the intensity distribution for each step of defocus:

$$I(r) = I_0 \frac{2J_1\left(\frac{1.22\pi}{\Delta x}x\right)}{\frac{1.22\pi}{\Delta x}x} + I_{offset}, \quad (3.2)$$

with  $J_1$  being the Bessel function of first kind,  $I_0$  the peak intensity,  $I_{offset}$  the intensity offset in the image,  $\Delta x$  the resolution according to the Rayleigh criterion and  $x$  representing the one dimensional coordinate. As a measure for the spot size the location of the 1. minimum ( $\Delta x$ ) has been chosen. The region along  $z$  where  $\Delta x$  is lower than the value at the focus times  $\sqrt{2}$

### 3. Lens Design

is defined as the DOF, see [Figure 3.6](#). It is important to note that the profile of the intensity distribution is theoretically predicted by [Equation 3.2](#) only in the direct vicinity of the focus. Outside the focus fitting this function only serves as a rough estimation for the overall spot size of the intensity. This is the reason why the parameter  $\Delta x$  gets smaller even beyond the position of best focus, as the intensity distribution of the images are not symmetric around the focus. In one direction a “smooth” spread of the peak occurs whereas in the other direction a narrow peak surrounded by dark and bright fringes emerges. In the latter case this leads to a reduced value of  $\Delta x$  due to the fit determining the first minimum of the multipeak structure. For the simulations OSLO determines the position of the focus automatically by finding the position along  $z$  with the least wavefront aberrations. However, for the measurements that are performed in the following chapter on the real imaging lens this is not possible, and deducing the focus from the spread of the intensity distribution is also tricky due to the asymmetry. Therefore the focus is determined by the position where the intensity distribution has the highest peak value. As shown in [Figure 3.7](#) for the case of the simulations the focus clearly corresponds to the position of highest peak value.

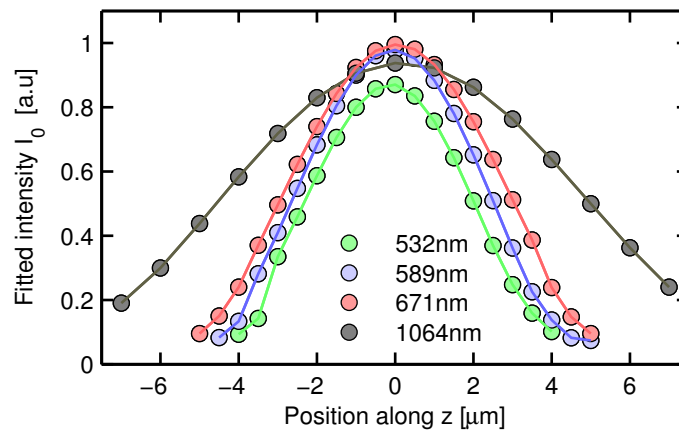


Figure 3.7.: Peak intensity of the PSF as a function of defocus for different wavelengths. In contrast to [Figure 3.6](#) in this graph the best focus position can clearly be determined as the highest value along the scan.

### 3.3. Tolerancing

So far the simulations have been carried out for a perfect system in a sense that all the parameters and positions have a defined value up to machine precision, which in terms of length scales is way below the picometer regime. Obviously such a precision can not be reached in a real system. Due to intrinsic technical limitations in the manufacturing process there is a tolerance associated with each surface and position parameter of the lens system. A real imaging lens will always resemble the theoretical design only up to a certain degree. Therefore it is an essential part of lens design to evaluate the performance of the lens design in terms of tolerance

values that are imposed on the system. A tolerancing analysis can be approached in different ways. One possibility is to set a certain performance value for the lens design and estimate the tolerances that can be accepted to ensure the performance criterion. The drawback of this method is that the influence of each toleranced parameter on the system performance has to be evaluated. Moreover the so determined tolerance might not be or only high priced realizable by the manufacturer. Therefore a statistical tolerancing analysis using Monte Carlo simulations has been chosen in the course of this thesis. The idea is to estimate the degradation of imaging

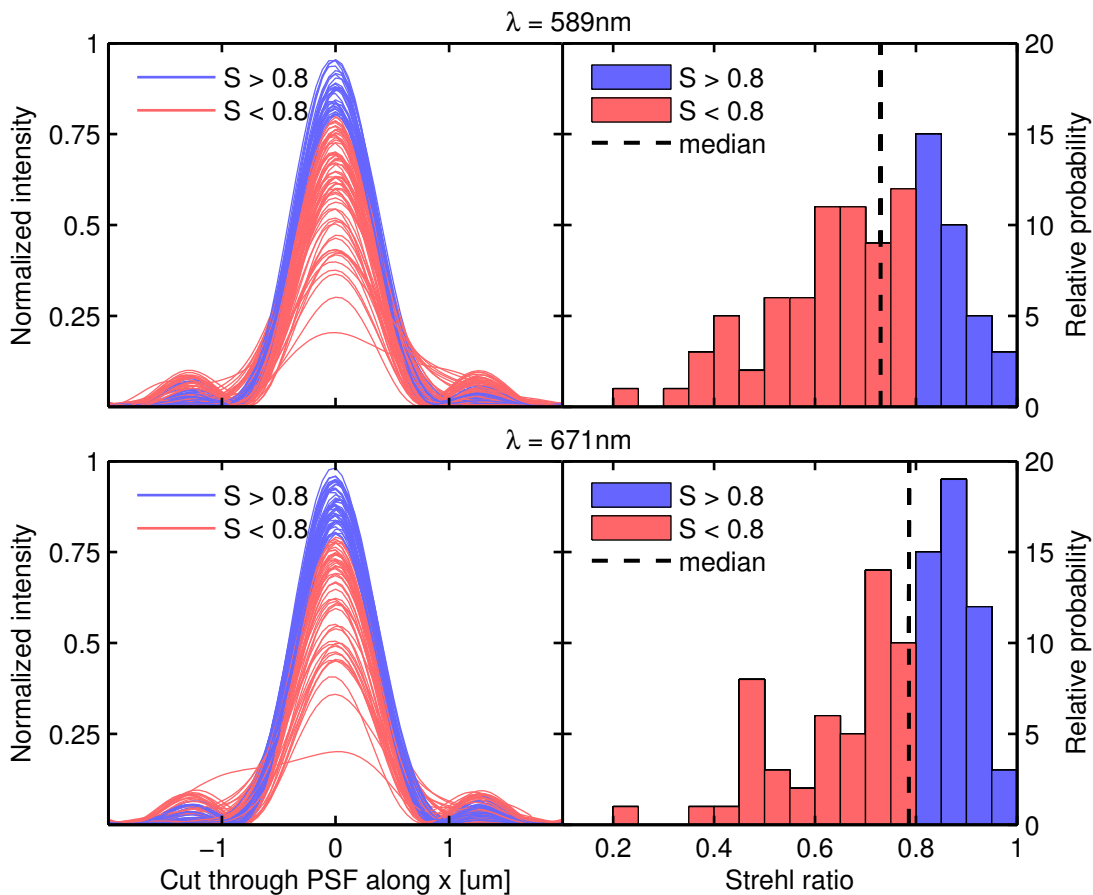


Figure 3.8.: Results of the Monte Carlo tolerancing of 100 simulated lens systems for  $\lambda = 589\text{nm}$  (**top**) and  $\lambda = 671\text{nm}$  (**bottom**).

**Left:** One dimensional profile of the PSF for each system is plotted, showing the diversity of imaging quality in all realizations. The cases where a Strehl ratio ( $S$ ) of 0.8 or higher is reached are marked in blue, otherwise in red. **Right:** Histogramm of the Strehl ratio taken from the corresponding left side graph. Clearly seen is the heavy tail behaviour of the distribution.

performance of the lens system under given tolerances. OSLO has a built in tool that randomly perturbs the lens system in each parameter within the limits of user-defined tolerances. By

### 3. Lens Design

evaluation of each perturbed system a statistical statement about the expected performance of a manufactured lens system can be made. For the analysis 100 perturbed systems were generated. The individual tolerances were set in accordance with the manufacturer LENS-OPTICS [12], they were chosen such that they can be achieved with moderate effort. As a measurable performance criterion the Strehl ratio has been chosen. Figure 3.8 shows a statistics summary of the perturbed systems. The simulation has been carried out for the imaging wavelength  $\lambda = 589\text{nm}$  (top) and  $\lambda = 671\text{nm}$  (bottom). On the left the evaluated PSFs of each perturbed system are shown. Curves that exhibit a Strehl ratio over 0.8 are printed in blue, otherwise in red. To the right a histogram of the Strehl ratio of each perturbed system is shown. The behaviour of not diffraction limited PSFs can be nicely seen in the plot. Not only is the peak value reduced but also the functional shape differs from the airy disc, clearly visible in the region of the second maxima. The Monte Carlo simulation emulates realistic manufacturing processes. The question that is answered with such an approach is the following: "Given the imaging lens is manufactured according to the design and the tolerances from above, how likely is it that the actual resulting imaging lens is diffraction limited?". We are interested in the number of lenses out of all simulated lenses that are diffraction limited. For  $\lambda = 671\text{nm}$  it amounts to 49% and for  $\lambda = 589\text{nm}$  it is 33%. It is up to personal judgement to regard these values as sufficient or not, however, it is important to note that this is an evaluation at full NA of the objective. Reducing the NA of the system by means of a variable aperture stop, one can restore diffraction limited performance as a tradeoff for best possible resolution. Figure 3.9 shows how a change of NA effects the number of diffraction limited systems in the Monte Carlo simulation. The NA was varied in steps by reducing the

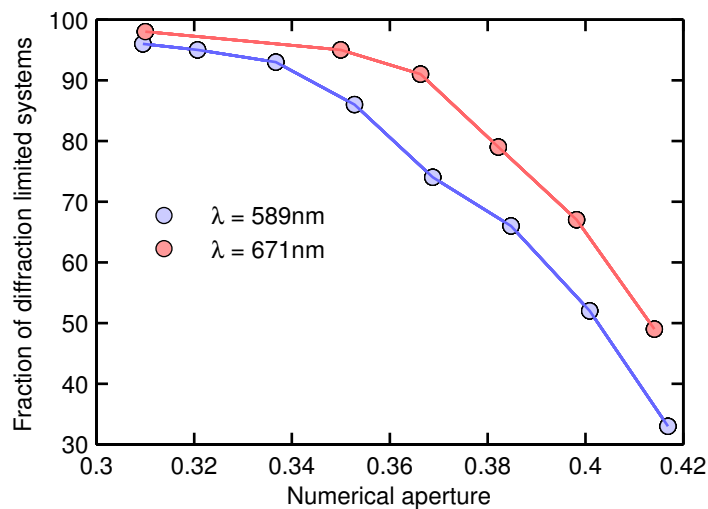


Figure 3.9.: Outcome of the Monte Carlo analysis as a function of varied NA for two wavelengths. For the datapoints the incoming clear aperture has been varied and 100 systems were simulated with the same tolerances as mentioned above. Solid lines are a guide to the eye

entrance beam diameter and for each value of the NA another MC simulation of 100 systems has been performed. For smaller NA the relative amount of systems with Strehl ratio of 0.8 or

higher increased. By reducing the NA to 0.34 the amount of diffraction limited systems reaches about 90%. This estimation is similar to the case described in [41]. Therefore we concluded that the lens design manufactured by LENS-OPTICS with their specific tolerances meets the requirements that we had in mind for the NaLi experiment.

### 3.4. Mounting

The NaLi imaging lens design as described above has been manufactured at LENS-OPTICS. The order comprised in total 4 sets of lenses. Two sets already mounted in a tube and two sets with just the individual lenses. The lenses have a customized antireflection coating in the range from 500nm to 1080nm. The two mounted lenses are used for the atom imaging and for imprinting optical potentials on the atoms. The two unmounted sets are used as backup and if necessary, a mount can be manufactured by the institutes workshop. The reason for ordering multiple sets is that the price for manufacturing customized lenses does not scale linearly with the amount of lenses. The grinding of the lenses as well as the coating are performed in machines that contain multiple lenses. The costly part is to set up and run the machines with customized parameters. Therefore one can get additional sets of lenses only for a fraction of the initial prize, as it is then only about, loosely speaking, inserting more blanks into the machines.

The tube mount was designed in accordance with the workshop of Lens-OPTICS keeping in mind the restrictions mentioned in [section 3.1](#). A sketch of the tube design is shown in [Figure 3.10](#). The tube consists of two parts, a front part where the lenses are mounted and a

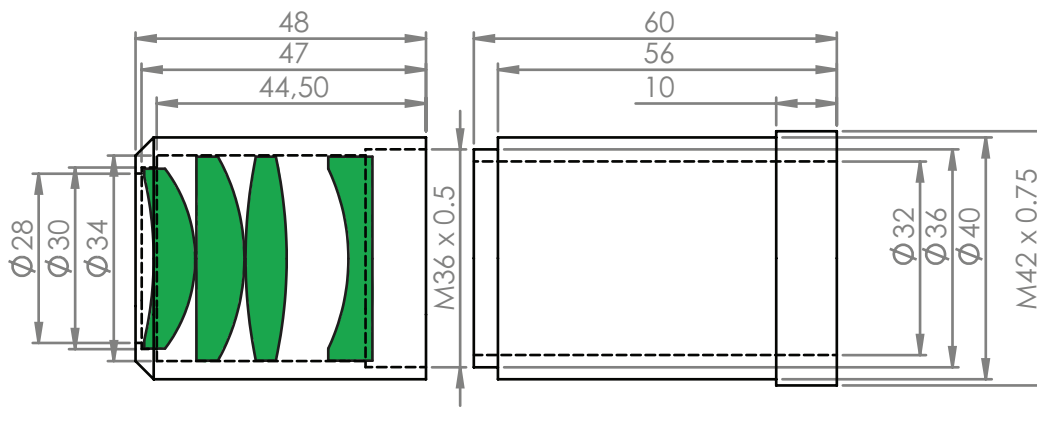


Figure 3.10.: Sketch of the lens tube design (scales in mm). The placement of the lenses is outlined in green. Not shown are the spacer and positioning rings. An external thread at the rear end enables attaching of the tube to alignment mechanics. In the front part the lenses are mounted whereas the rear part serves as an extension.

rear part that serves as an extension. The reason for a two part design is that a total length of about 10cm is necessary to support the tube from below in a place that is not obstructed by the magnetic trap coils. However, manufacturing a tube of this length bears the risk that the tube walls exhibit residual slope which complicates the precise centering of the lenses.

### 3. Lens Design

The rear end of the tube features an external thread for attaching the tube to alignment mechanics. To align the imaging lens properly in the experiment a kinetic mount with three translational and two rotational degrees of freedom is necessary. The imaging setup as proposed in [Figure 3.4](#) includes in addition to the imaging lens at least four more optical elements (two mirrors, two secondary lenses). Since all this optics need 5 degrees of freedom for alignment, we decided to build a compound mount that accomodates all these optics at once. Within this mount the optic elements are placed rigid and aligned according to an internal optical axis (defined by the symmetry axis of the objective). Therefore only one 5-axis alignment stage is needed that adjusts the position of the compound mount as a whole. Such a mount was designed in the course of this thesis and manufactured by the mechanics workshop of the Kirchhoff Institute. A technical drawing of this mount is shown in [Figure 3.11](#) which will be referred to as the “TOWER” in the following.

The design criteria for the TOWER were stability, shielding of the optics, versatility in change of optics and convenient implementation into the experiment. The design features four openings for optical access. At the top opening the imaging objective is positioned by means of an M42 x 0.75 internal thread. The rotational symmetry axis of the lens tube defines the optical axis of the TOWER. The two upper openings on the side are intended for the secondary lenses that form the final image on the cameras. The lenses are mounted by means of a Thorlabs 60mm cage system. The cage system is a very flexible tool for conveniently replacing of the secondary lenses as well as adding other optics (filters, iris) in the imaging path. The lowest opening is designed for injecting the dipole trap beam. As shown in [Figure 3.11](#) the dipole beam propagates contrary to the imaging beams direction. Inside the tower three mirror holder are placed. The upmost mirror is a dichroic mirror that deflects the imaging light of sodium (589nm) and passes the imaging light of lithium (671nm). The next mirror is another dichroic mirror that deflects the lithium imaging light. Both dichroic mirrors are transparent for the infrared dipole trap beam (1064nm). All mirrors are placed in 45° with respect to the optical axis which hits the center of the mirrors. As indicated in [Figure 3.11](#) the position of the mirror holder is chosen such that it compensates the transversal shift of the optical axis when passing through the tilted bulk material of the dichroic mirrors. The TOWER is placed on two alignment stages. First is a home built tilting stage that is translated with three micrometer screws with a total travel of 25mm. The tilt in x and y direction is set with this platform. Moreover by turning all three screws in the same direction the linear translation along z can be set. The second stage is a commercial two axis linear translation stage (Newport M-401) with a total travel of 12.7mm in each direction. The displacement from the optical axis in x and y direction is set with that stage. To avoid that the lens tube is mechanically moved too close to the glass (and scratching it potentially) a protective spacer is placed around the lens tube. This spacer will hit the magnetic trap coils and prevent further upmovement of the TOWER when the outer edge of the lens tube is 4 mm close to the vacuum cell. The TOWER is made out of black eloxed aluminum to reduce stray light in the imaging path.

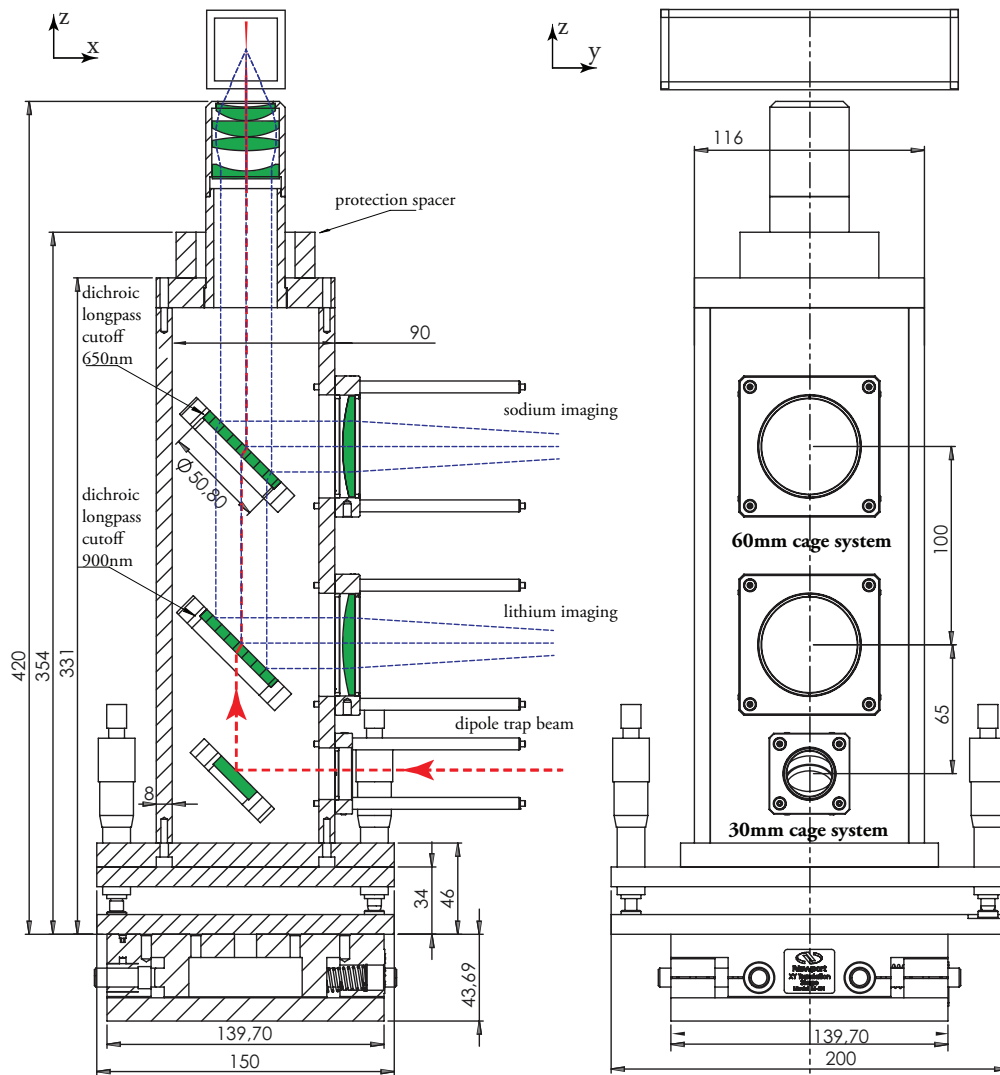


Figure 3.11.: Technical drawing of the TOWER. The main body is a rectangular box with four round openings for optical access. At the top opening the imaging lens tube is mounted and its rotational symmetry axis defines the optical axis. The inside of the TOWER contains three mirror holder that are placed in  $45^\circ$  relative to the optical axis. The two upper mirrors are 2-inch dichroic mirrors (Thorlabs DMLP650L and DMLP900L), the lowest one is a 1-inch metallic mirror (Thorlabs PF10-03-P01). The secondary lenses are mounted on Thorlabs 60mm cage system plates. The TOWER is placed on a home built three micrometer screw (Mitutoyo 150-801) tilting platform and a commercial two axis linear stage (Newport M-401/SM-13). The lowest opening and the metallic mirror serve as an input for the dipole trap beam.



## 4. Characterization of the Imaging System

Before replacing the imaging objective on the experiment with the new one, an in depth analysis of the imaging properties of the lens and the functionality of the TOWER has been performed in a test setup. On the one hand it has been evaluated how far the performance of the imaging lens is consistent with the simulations performed with OSLO as described in [chapter 3](#). On the other hand the handling of the TOWER has been tested to develop an effective alignment procedure that can also be applied in the experiment.

### 4.1. Test Setup

A test setup that emulates the conditions of the experiment has been built on a separate optical table, see [Figure 4.1](#). A test pattern was illuminated with a collimated beam of either 589nm or 671nm wavelength. A glass plate of the same thickness and material as the vacuum cell has been placed 16mm after the test pattern to simulate the effects of imaging through the vacuum cell. Test images were taken with secondary lenses of different focal lengths (200mm/400mm/1000mm). For the evaluation of imaging performance mainly the measurements with the  $f = 1000\text{mm}$  lens have been used as it provides the highest magnification. The images were captured on a CCD camera (Guppy GF 46B) and saved as bitmap files. For data treatment the files were loaded into MATLAB and evaluated with self written analysis routines. Cameras and test pattern were mounted on xyz alignment stages (camera stage graduation:  $10\mu\text{m}$ , test pattern stage graduation:  $2\mu\text{m}$ , compare [subsection 4.2.3](#)). The test pattern was a gold foil with periodically positioned holes in x and y direction. The holes have a diameter of 650 nm and are spaced by  $20\mu\text{m}$ , for further details see [33].

Alignment of all components according to the optical axis is crucial for reasonable image formation. After many trials the following alignment procedure has shown to be the most reliable in the test setup:

1. **Align the fiber output coupler such that the imaging beam is parallel to gravity:** For that purpose we use a commercial laser level used for construction purposes (Conrad SuperCross-Laser 2 Laserliner 081.120A) with a precision of 0.5 mrad according to the manual. Moreover one has to make sure that the imaging beam is collimated.
2. **Align the tilting platform perpendicular to the imaging beam:** The TOWER is removed from the tilting platform and a mirror is placed in the center where the imaging beam hits the platform. The reflected beam from the mirror can now be steered back into the output coupler by aligning the platform with the micrometer screws. Then the reflected beam is coupled into the fiber good perpendicular alignment is achieved.

#### 4. Characterization of the Imaging System

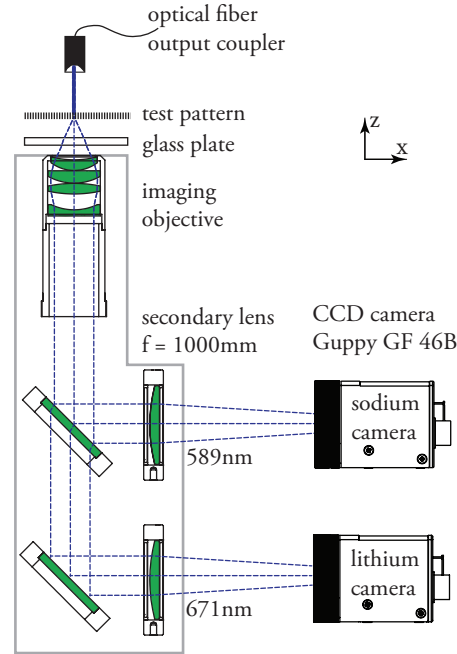


Figure 4.1.: Sketch of the setup for testing the imaging lens and TOWER. A test pattern is illuminated with imaging light of 589nm or 671nm. 16mm after the test pattern a glass plate with same properties as the vacuum cell is placed. The TOWER (framed in light grey) is aligned according to the procedure in the text. The images are recorded on CCD cameras (Guppy GF 46B). Real pictures of the test setup and test pattern can be found in the Appendix.

3. **Position the TOWER without optics coarsely:** The optic components are removed and the body of the TOWER is positioned on the tilting platform. TOWER and alignment stages are moved roughly so that the imaging beam enters central in the top of the TOWER.
4. **Place mirrors in 45° angle:** The mirror holders have a residual play when they are fastened in place. Therefore while tightening the screws of the mirror holder one has to ensure that the imaging beam is deflected in a right angle, this can conveniently be done with the laser level.
5. **Align the TOWER's geometrical optical axis onto the imaging beam:** The displacement of imaging beam and optical axis can be seen when a cage alignment plate (Thorlabs LCPA1) is placed on the cage rods. The deviation of the beam spot from the crosshair center marks the displacement in x and y from the optical axis. With the linear xy translation stage at the bottom this deviation can be compensated.
6. **Position the cameras:** The cameras are placed such that the deflected beam hits centrally on the CCD chip. The exact distance of the camera from the tower is determined by placing the secondary lens in the designated position in the cage system. When the

previous alignment has been done properly the spot on the CCD camera should not have moved. The desired position of the camera is the focus plane of the secondary lens.

7. **Place the imaging objective:** When mounting the top plate containing the imaging lens one has to pay attention to the amount of play when fastening like it happens with the mirror mounts. In this case one has to make sure that the beam spot on the camera, although strongly expanded, has its central position at the same place as before the imaging lens placing.
8. **Position the imaging object:** The test pattern is slid into the imaging beam, since it is a periodic structure that extends over a couple of millimeters, a certain part of the structure is inside the FOV of the imaging lens and xy alignment is less critical. The z position of the gold grating has been scanned to find the best focus.

An important detail has to be mentioned here regarding the used gold grating: Due to the Talbot effect [6] images of the illuminated gold grating are reproduced in the near field of the grating. One has to ensure that the actual grating is in the focal plane of the imaging lens and not a Talbot image. This can be done with help of rectangular holes of several hundred micrometers. These are positioned on the gold foil sufficiently far apart from the grating structure. For such a hole the Talbot effect does not play a role and a sharp image is formed only in the focus plane of the imaging lens. Therefore the procedure of focus search was to position the rectangular hole on the imaging beam and find a sharp image, then slide the gold foil over where the grating structure is illuminated. The image formed in this vicinity is assured to be the “real” grating.

## 4.2. Image Analysis

For image analysis the pictures have been imported into MATLAB, see [Figure 4.2](#). The gold grating was mounted on a xyz translation stage enabling easy scan through the focus as well as locating the same position within the grating. In the test setup both mounted imaging objectives were tested (hereafter labeled objective 1 and objective 2). If not specified further in the text, in the following the data of objective 1 using the sodium wavelength  $\lambda = 589\text{nm}$  are discussed. Since the imaged object is a grating with defined periodical structure, the full view images ([Figure 4.2](#) top) can be conveniently used to determine the magnification and FOV of the system. For analysis of the imaging performance and resolution of the objective, one single hole of the grating has been picked, [Figure 4.2](#) bottom. Attention has been paid to always pick the same hole as marked by the white box. This could be done by counting the rows and columns of the grating starting from the edge of the whole structure. An analysis of the PSF has been performed on the single hole’s image. The case in which the image of one single hole corresponds to the PSF of the system holds when the hole represents a point-like source i.e. when the diameter of the hole is smaller than the extent of the system’s PSF. If not, the image will be spread according to [Equation 2.15](#). To estimate the effect of the 650nm hole size used in the test setup the following simulation has been carried out: The coherent imaging process was simulated by convolving and squaring holes of different diameters with the APSF (see [Equation 2.11](#)) of the imaging objective at 589nm. The resulting images were compared to the PSFs of the imaging

#### 4. Characterization of the Imaging System

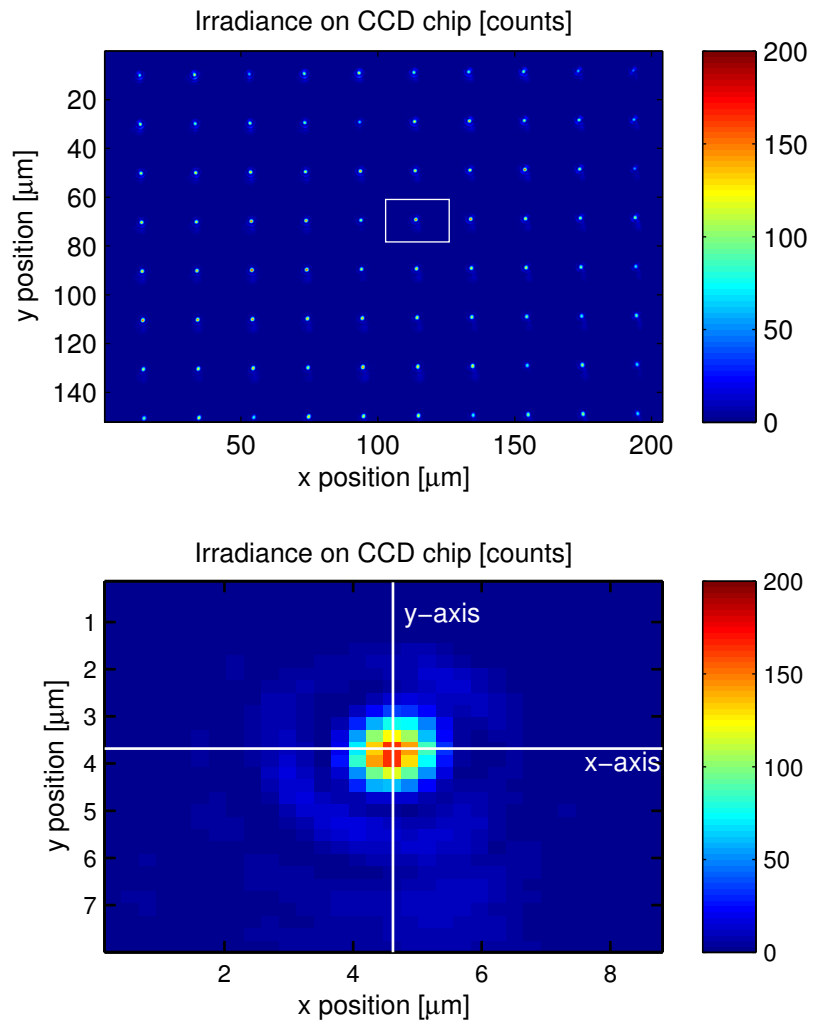


Figure 4.2.: **Top:** Image of the gold grating recorded with the sodium camera. Laser power and camera exposure time were chosen such that the camera stays below saturation (255 counts). The white box marks the single hole that is shown below. **Bottom:** Cropped section of a single imaged hole that is used for analysis of the PSF. The white lines mark the cut along which the 1-dimensional fits were performed.

objective. The results are shown in [Figure 4.3](#). The finite hole size of 650nm causes a shift of the 1. minimum of 3.7% compared to the perfect Airy disc (2.8% when imaged with 671nm). This corresponds to a decrease of the Strehl ratio of 1.1% even in the absence of aberrations. The Strehl ratio was computed according to [Equation 2.18](#) (here, the simulated intensity pattern was renormalized to the total intensity of a perfect Airy disc, thus the decrease in Strehl ratio). Therefore the imaged holes cannot strictly be considered point-like, however, the effects can be regarded as a small biased perturbation. Moreover the values mentioned above are worst case assumptions, as for reduced NA of the system these effects get smaller. Hence in the following

it is assumed that the image of a single grating hole represents the PSF of the imaging system.

#### 4.2.1. Magnification

The image showing multiple holes can be used to determine the magnification of the imaging setup. The CCD camera has a chip comprised of  $752 \times 580$  pixels with individual pixel size of  $8.6\mu\text{m} \times 8.3\mu\text{m}$  and the grating holes are separated by  $20\mu\text{m}$ . The distance between multiple holes was manually measured in pixels and compared to the corresponding distance in object space. From this a magnification of  $M_x = 31.72 \pm 0.07$  in x direction and  $M_y = 31.66 \pm 0.08$  in y direction was determined. The error reflects the uncertainty of one pixel when manually determining the center of the hole by the pixel of highest irradiance. Theoretically the magnification is given as the focal length ratio of secondary and objective lens, see Equation 3.1. For  $f_{\text{objective}} = 31.18\text{mm}$  and  $f_{\text{secondary}} = 1000\text{mm}$  this yields  $M_{\text{theo}} = 32.07$ . As described in subsection 3.2.1 the gold grating is positioned in the focus for imaging light of  $589\text{nm}$ , therefore the lithium imaging path deviates from the infinity corrected configuration and exhibits larger magnification. The determined values are:  $M_x = 37.56 \pm 0.10$  and  $M_y = 37.45 \pm 0.15$ . A ray analysis with OSLO yielded a magnification of  $M_{\text{OSLO}} = 37.31$ .

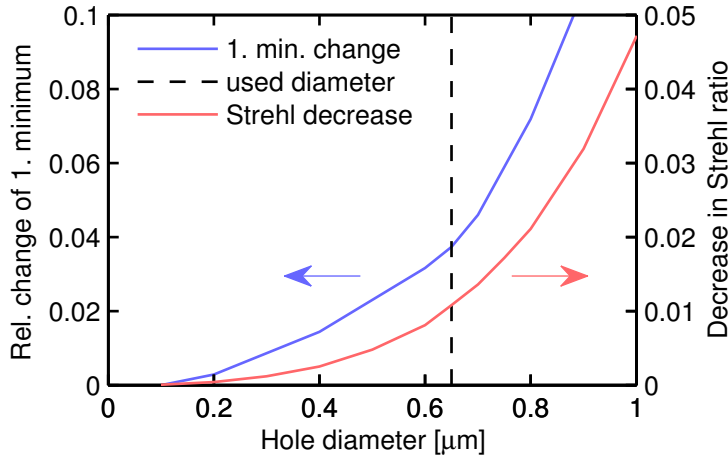


Figure 4.3.: Comparison between the PSF of an imaging system and the coherent image of an object with varying dimension. The simulation has been carried out for the imaging lens with  $\text{NA} = 0.417$  and  $\lambda = 589$ . For increasing hole diameter the PSF spreads out, observable by a shift of the location of 1. minimum of the airy disc (blue line). Associated with that spread is also a decrease of the Strehl ratio (red line), as the effects of aberration is a distribution of intensity from the peak to the wings.

#### 4.2.2. PSF analysis

The PSF has been the main object of observation during the tests as it provides a very descriptive measure of imaging performance. Already with bare eye one can distinguish if the image is in good focus or not. Moreover, the appearance of dominant fringes or a deformation of the main

#### 4. Characterization of the Imaging System

peak indicates misalignment of the tower or wrong positioning of the camera.

For quantitative analysis of the images a fitting routine has been applied. Due to the low amount of pixels on which the peak feature is spread out, fitting a two dimensional Airy disc did not converge reliably. Therefore a fit of the form as in Equation 3.2 has been used for the one dimensional profiles along x and y through the peak of the single hole image (as indicated in Figure 4.2). The fit according to the x cut in Figure 4.2 bottom can be seen in Figure 4.4.

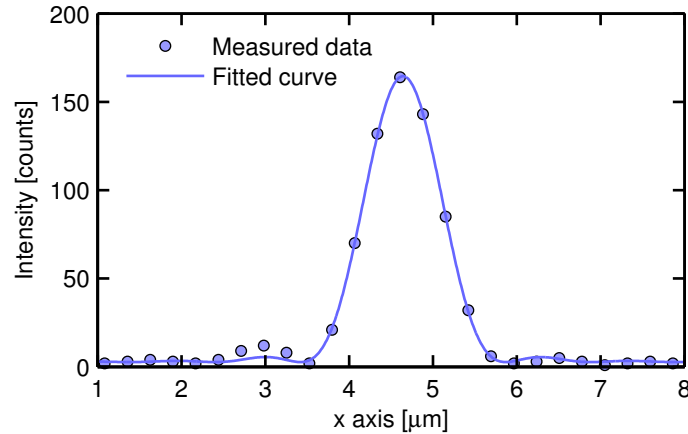


Figure 4.4.: One dimensional cut through the peak of a single hole image along x direction and fitted curve of the form as in Equation 3.2.

#### 4.2.3. Determining the Best Focus

An analogous analysis to the one shown in Figure 3.6 has been performed to determine the best focus position for the imaging. Here the gold grating has been moved along the z-axis by means of a manual translation stage with a micrometer screw (Mitutoyo 148-142). The movement has been done in steps of  $2\mu\text{m}$  which corresponds to the graduations on the screw. At each position an image was recorded and analyzed as described above. The results of such a focus scan are shown in Figure 4.5. According to the findings in subsection 3.2.2 the position of focus is characterized by a clear maximum in intensity in a range along z that is on the order of the DOF. This is not the case for the test measurement as it shows another distinct maximum around  $28\mu\text{m}$  next to the main maximum at  $14\mu\text{m}$ . This behaviour can be understood by looking at the raw pictures along the scan that are shown in Figure 4.5 bottom. To the left side of the main intensity maximum the PSFs are “blurred” which is the naive expectation for an image out of focus, whereas to the right side a narrow peak surrounded by fringes appears. This asymmetry around the focus is also seen in Figure 3.6, however, in the test measurements the narrow peak inside the fringes carries a significant amount of intensity.

These observations can be explained by the presence of spherical aberrations in the imaging lens. Spherical aberrations produce rotational symmetric image defects around the axial image point [7]. Those are clearly seen in the raw images. Moreover spherical aberration cause axial rays and marginal rays to focus at different distances along the optical axis explaining the large

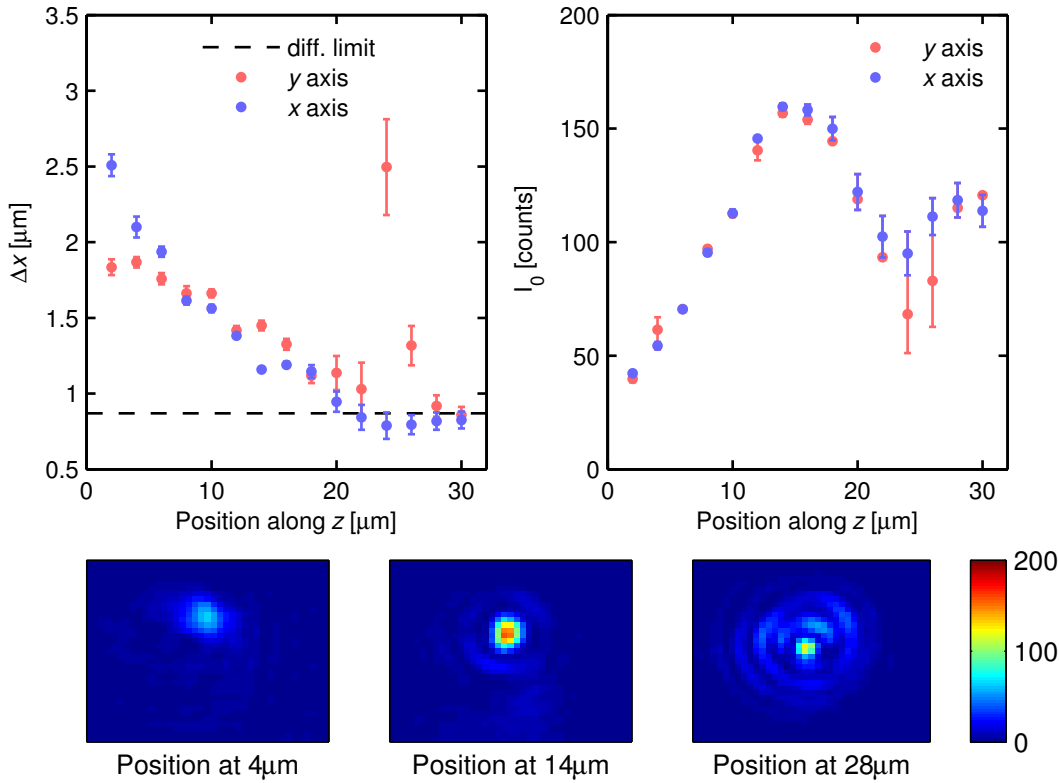


Figure 4.5.: Single hole images analyzed for different positions of the gold grating along the optical axis  $z$  at full NA and imaged with  $\lambda = 589\text{nm}$ . **Top left and right:** Fitting parameters  $\Delta x$  and  $I_0$  determined with the method described in subsection 4.2.2. The errorbars represent the 0.67 confidence bound determined by the fitting routine. The sharp peak in  $\Delta x$  at  $24\mu\text{m}$  is an artifact of fitting, since in this region the intensity profile along one axis has a multipeak structure that cannot be properly treated by fitting an Airy profile. **Bottom:** Raw images taken along the  $z$  scan. The structure seen at  $28\mu\text{m}$  is a strong hint that spherical aberrations are dominant. The raw images represent  $10.57\mu\text{m} \times 9.18\mu\text{m}$  in object space.

distance along  $z$  on the right side of the scan where the intensity stays high (peak intensity does not drop below 59% of the maximum). Therefore the point at  $14\mu\text{m}$  in the scan is not the best focus in the sense of a diffraction limited system but rather the circle of least confusion [21] which represents in an aberration limited system the  $z$  position of smallest geometrical spot size. Hence the position of 1. minimum  $\Delta x$  at scanning point  $14\mu\text{m}$  does not agree with the expected value for a diffraction limited system at this NA.

To make a systematic check whether the dominance of spherical aberrations is a reasonable explanation for the observations, the same focus scan measurement has been performed for the system with reduced NA. Since spherical aberrations increase for rays outside the paraxial region, they can generally be reduced by stopping down the clear aperture. An iris with variable

#### 4. Characterization of the Imaging System

diameter has been used to vary the clear aperture of the imaging lens and thus changing the NA. Figure 4.6 shows the summarized results of a focus scan performed with a clear aperture

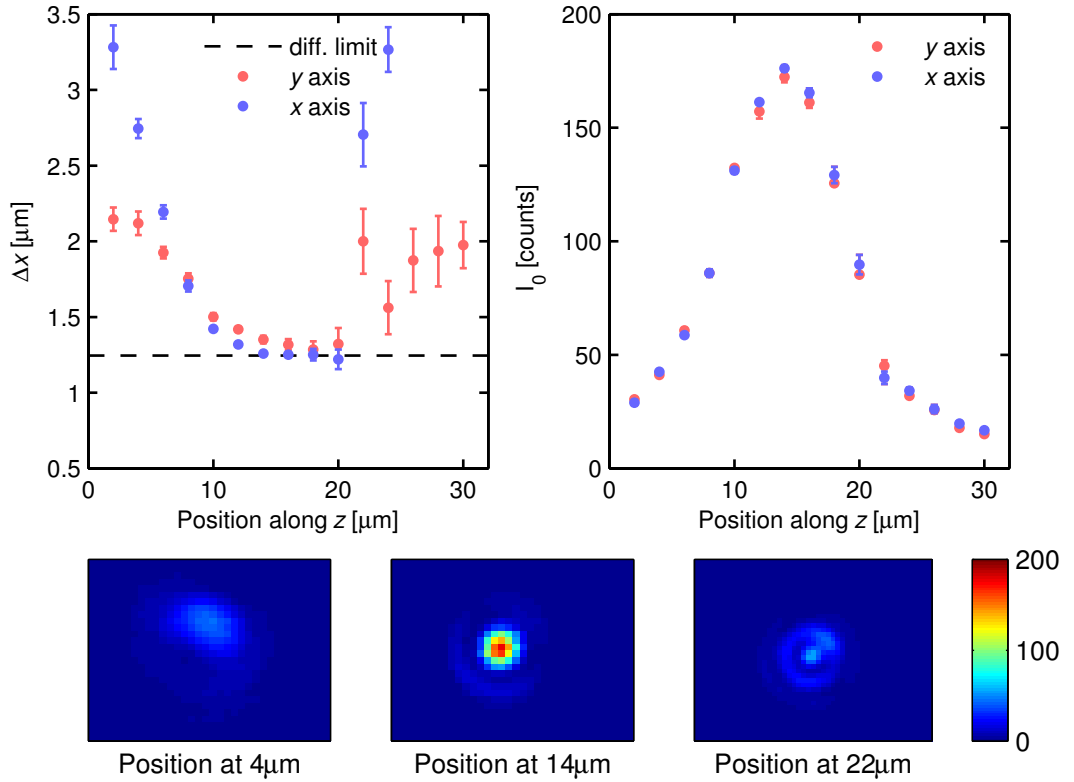


Figure 4.6.: Same analysis as in Figure 4.5, but with reduced NA of 0.29. The top right plot now clearly shows only one maximum at  $14\mu\text{m}$ . Moreover there are no more dominant fringes in the raw data as seen in Figure 4.5. The raw images represent  $9.21\mu\text{m} \times 7.34\mu\text{m}$  in object space.

of 18mm corresponding to an NA of 0.29. For this scan a clear focus at  $14\mu\text{m}$  is determined as the peak intensity is symmetric around  $z$  and has a clear maximum. Qualitatively the peak intensity and  $\Delta x$  curve in the case of lower NA agrees much better with the simulated results in Figure 3.6 and Figure 3.7. An asymmetric tendency around the focus can still be seen in the raw pictures, however, the peak intensity drops equally in both directions away from focus. Moreover now the value for  $\Delta x$  at focus is in agreement with the predicted diffraction limited value given by Equation 2.17.

We concluded from these observations that the imaging lens suffers from spherical aberrations when used at full NA. As expected, these aberrations can be reduced by reducing the NA with an iris which can be conveniently implemented into the cage system of the TOWER. Moreover the imaging properties of the system have to be considered as a function of the NA and it is up to the particular circumstances of the experiment which NA to choose as a most suitable “working point”.

#### 4.2.4. Depth of Field (DOF)

Determining the DOF in a straight forward fashion is complicated by the fact that the intensity distribution around the focus in  $z$  direction exhibits strong asymmetry. Therefore the common definition of the DOF as the Rayleigh length does not seem well suited. Moreover the scan has been performed in steps of  $2\mu\text{m}$  (limited by the precision of the micrometer screw of the translation stage) which makes a precise determination of the DOF all the more difficult without an analytic prediction at hand.

Therefore we make an estimation of the DOF as the region along  $z$  where the fitted intensity stays above 60% of the peak intensity. This definition reflects the width of the main intensity maximum in [Figure 4.5](#) and is hence regarded as an appropriate measure to describe the region of considerably good focus in our system. The so determined values for the DOF are shown in [Figure 4.7](#) as a function of NA. Although the DOF is only roughly estimated, it yet provides

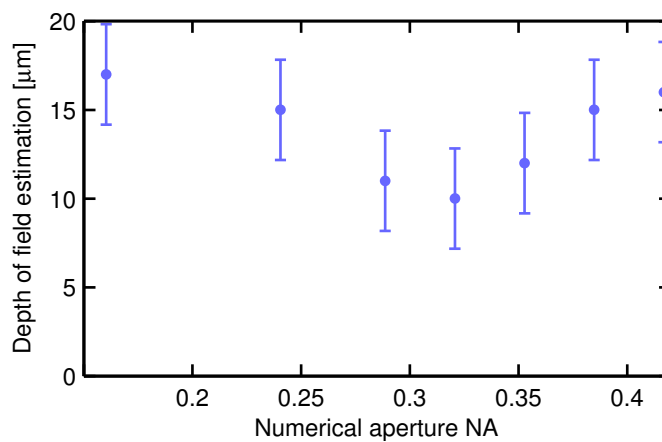


Figure 4.7.: DOF as defined in the text for different NA. The errorbars reflect the uncertainty due to manual estimation of the DOF given the  $2\mu\text{m}$  step size of the focus scan. Although being just a rough estimation, the graph provides insight about the order of magnitude of the DOF as well as the region around 0.32, where spherical aberrations become dominant.

two important informations: First, the order of magnitude of the DOF can be predicted to be tens of micrometers. This sets the required precision of the alignment mechanics, which is fulfilled by the TOWER. Moreover it can be assumed that the imaging system is rather stable to mechanical drifts and does not require frequent readjustment of the focus as it is the case for imaging lenses with DOF on the order of a few micrometers [27]. Second, the DOF as a function of NA displays a minimum in the region around 0.32. For a system free of aberrations one expects a decrease of DOF for large NA [21]. Therefore the minimum in [Figure 4.7](#) marks the region where aberrations get dominant with increased NA.

### 4.2.5. Resolution

The resolution according to the Rayleigh criterion is the distance between peak position and 1. minimum of the airy disc. In the used fitting routine described above, this corresponds to the parameter  $\Delta x$  for a fit of a single hole image in focus. Strictly speaking this definition assumes the case of a diffraction limited system. For an aberrated system the PSF is in general no perfect Airy disc any more. As a common criterion for the diffraction limit the presence of aberrations up to a small amount is taken ( $OPD_{rms} < 0.07$ ). In this limit considering the PSF as an Airy disc is still reasonable. For larger aberrations the shape of the PSF changes stronger, depending on the type of aberration. A descriptive empirical example can be seen in the Monte Carlo tolerancing simulations (Figure 3.8, left), there the effect of many possible aberrations is displayed. In general stronger aberrations manifest in a broader and lower main peak of the PSF and more intensity located in the side fringes as well as the appearance of radial and lateral asymmetry of the PSF.

Resolution in the following is considered as the parameter  $\Delta x$  determined by the fitting procedure described in subsection 4.2.2 and taken at the best focus position according to subsection 4.2.3 disregarding the strict prerequisite of the Rayleigh criterion. In order to evaluate up to what extent resolution in that sense is diffraction limited it is compared to the theoretical prediction of diffraction limited resolution for given NA described by Equation 2.17. For non diffraction limited systems one expects a broadened PSF and thus a resolution  $\Delta x$  larger than the theoretical prediction. The evaluated resolution as a function of NA is shown in Figure 4.8. The experimental data lies in the vicinity of the theoretical diffraction limit for NA values up to about 0.35. For higher NA there is a clear deviation from it. This is in accordance with the observations of the previous sections that for high NA spherical aberrations play a dominant role. Another noticeable characteristic of the graph is that for NA values of 0.25 and higher the values of  $\Delta x$  along x and y axis are offset, although both show the same functional behaviour with its minimum at around 0.35. The reason for that discrepancy couldn't be determined yet during the test measurements. An individual rotation of the optical components in the imaging path (imaging lens, dichroic mirror, secondary lens) rendered the same result. From that we conclude that this breaking of symmetry is not intrinsic to the optics. A strong indication for a preferred axis is the system layout using dichroic mirrors. The dichroic mirrors are tilted by 45° around the x axis (here it is referred to the x axis as defined in Figure 4.2, not to be confused with the x axis of Figure 4.1). Maybe the different clear aperture along x and y due to the tilt has an effect, which on the other hand should not play a role since the reduced clear aperture along the y axis of 35.92mm is still clearly large enough to cover the outgoing collimated beam of the imaging lens which has a diameter of 26mm. Another suggestion is the influence of the dichroic mirror on the polarization of the imaging light. The used dichroic mirrors have different transmission and reflectance coefficients for p and s polarized light (see DMLP650L [13]). The imaging light has not been analyzed regarding the polarization and therefore an influence of the polarization on the imaging can't be ruled out. These suggested influences are inherent to the layout of the TOWER using tilted dichroic mirrors and can easily be tested for their validity in a setup with no deflecting dichroic mirror in the imaging path.

The values for the resolution taken at NA = 0.35 are summarized in Table 4.1.

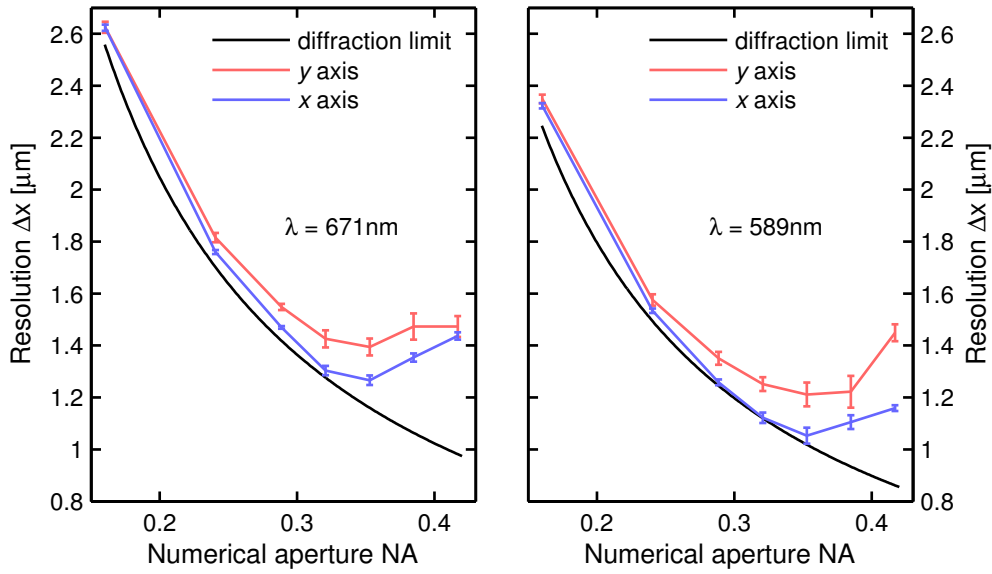


Figure 4.8.: Resolution defined as the fitting parameter  $\Delta x$  at best focus, as a function of NA. The errorbars represent the 0.67 confidence bound determined by the fitting routine. The resolution of the y axis is offset compared to the one along x, possible explanations for that are discussed in the text. Up to an NA of 0.32 the resolution along the x axis is in good agreement with diffraction limited resolution. The deviations from the diffraction limit is in accordance with the observation of dominant spherical aberrations for higher NA. The solid lines are guides to the eye.

Numerical Aperture	Imaging wavelength [nm]	Measured resolution along x [ $\mu\text{m}$ ]	Measured resolution along y [ $\mu\text{m}$ ]	Diffr. limited resolution [ $\mu\text{m}$ ]
0.35	589	$1.05 \pm 0.03$	$1.21 \pm 0.05$	1.02
0.35	671	$1.27 \pm 0.02$	$1.39 \pm 0.03$	1.16

Table 4.1.: Summary of the experimentally determined resolution at the minimum in [Figure 4.8](#) (NA = 0.35).

#### 4.2.6. Field of View (FOV)

Having the gold grating as the test pattern for imaging also aids in determining the FOV of the imaging lens. By aligning the TOWER and camera such that the best imaging properties are achieved for the grating holes in the center portion of the CCD chip, one can observe the deterioration of the individual PSFs with larger distance from the center. Such a measurement has been performed with a secondary lens of 20cm focal length rendering a Magnification of 6.34. With this magnification a larger amount of single holes has been able to be imaged on the camera. Such a raw image of the grating is shown in the left of [Figure 4.9](#). To quantitatively analyse that

#### 4. Characterization of the Imaging System

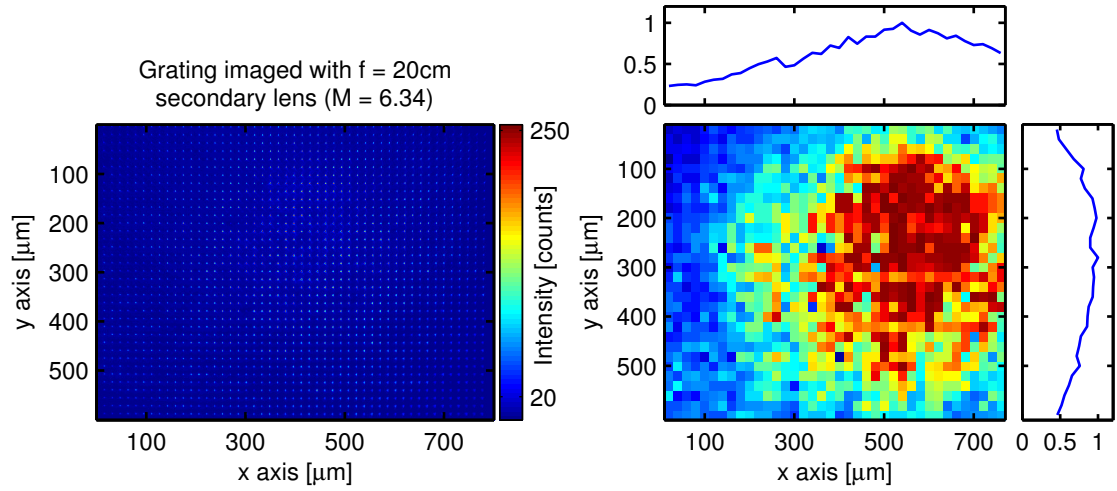


Figure 4.9.: Analysis of the FOV. **Left:** Image of the grating taken with lower magnification (6.34). **Right:** The fitted intensity of each hole mapped onto the grating position (intensity map). The integrated and normalized profile of the intensity map along the y and x axis are attached at the top and left. As the FOV we estimate the distance where the intensity stays above 0.8 of the maximum.

image the individual holes are fitted with function [Equation 3.2](#). The so determined  $I_0$  for each hole is displayed on a map representing the hole's position in the grating ([Figure 4.9](#) right). This map clearly exhibits an area of good image quality inferred from the center peak height of the PSF. To avoid influence of the imaging laser beam's intensity profile on this measurement the beam has been expanded with a two lens telescope largely to ensure approximately homogeneous intensity across the grating area of interest. The integrated and normalized profiles of the map along the y axis (x axis) are shown to the top and right of the intensity map. As the FOV we estimate the region where the intensity stays 0.8 and higher (compare [subsection 3.2.2](#)). This yielded a  $\text{FOV}_x = (240 \pm 28)\mu\text{m}$  and  $\text{FOV}_y = (320 \pm 28)\mu\text{m}$ , the errors represent the uncertainty due to the manual estimation of the 0.8 region in steps of  $20\mu\text{m}$ . These values are just rough estimations due to two reasons: Firstly, as has been shown in the previous sections the used NA of the system is a parameter that can greatly influence the imaging properties of the system. The image of [Figure 4.9](#) has been taken at full NA without optimizing for neither resolution nor FOV. Secondly the definition of 0.8 as a boundary for the FOV was taken referring to the simulations in [subsection 3.2.2](#) considering the relation between  $\text{OPD}_{\text{rms}}$  and Strehl ratio. In the case of this measurement the reduced Strehl ratio of the peak hole PSF was not taken into account.

### 4.3. Conclusion on Tested and Designed Properties

Having done the test measurements the general conclusion is that the properties of the imaging lens are in agreement with the design criteria within the expected fluctuations of the lens

### *4.3. Conclusion on Tested and Designed Properties*

parameters during the manufacturing process. As described in the tolerancing procedure of [section 3.3](#) the designed diffraction limited performance can be reached in the manufactured lens only with a limited probability. Equivalently one can state that (see [Figure 3.9](#)) the manufactured lens will reach diffraction limited performance more likely for lower NA. We explain the behaviour seen in [Figure 4.8](#) with exactly this tolerancing consideration. Only for NA values below 0.35 the measured resolution approaches the diffraction limit. The measurements of the DOF and FOV have been less sophisticated and should be regarded as estimations for the order of magnitude. An evaluation of the system's magnification yielded agreement with the predicted values by simulations with OSLO. Although not shown explicitly in this chapter, the imaging property tests have been performed on both manufactured and mounted imaging lenses. All tested values are similar within few deviations of about 10%.



## 5. Conclusion and Outlook

This thesis reports on the design and implementation of an imaging objective for imaging cold atomic clouds of sodium and lithium. The objective has been designed with the raytracing software OSLO. The design process incorporated the specific requirements of the NaLi experiment. This included that the imaging lens performs for a wide range of wavelengths (532nm, 589nm, 671nm, 1064nm) and enables diffraction limited performance for high NA (0.41).

A specific mounting device (TOWER) has been constructed that provides mounting and alignment mechanics for the imaging objective as well as secondary optical elements that are included in the imaging path.

Test measurements on a separate setup have been performed to assess the properties of the imaging system. The tests included the imaging of point like holes in a test pattern that could be used to analyse the PSF of the imaging system. The evaluation yielded performance close to the diffraction limit at a NA of 0.35, which is in good agreement with a conducted tolerancing analysis.

Shortly before the submission date of this thesis the new imaging setup has been built into the NaLi experiment. [Figure 5.1](#) Shows the first images of atomic clouds of sodium that have been imaged with the new objective. The pictures were taken by means of absorption imaging. The

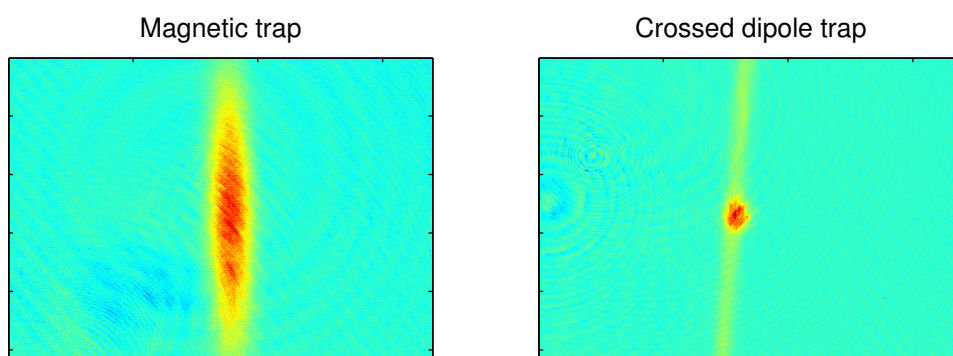


Figure 5.1.: First absorption images taken with the new objective. **Left:** Cloud of sodium atoms in the magnetic trap after evaporation (time of flight:  $20\mu\text{s}$ ). **Right:** Cloud of sodium atoms in the crossed dipole trap (time of flight:  $500\mu\text{s}$ ). Since the calibration of the magnification has not been done yet, there is no reliable length scale for the images yet.

left hand side shows a cloud of sodium atoms in the magnetic trap after evaporation. The right hand side shows a cloud of thermal sodium atoms that were loaded from the magnetic trap into the crossed dipole trap. A detailed explanation of the different stages of the experimental

## 5. *Conclusion and Outlook*

sequence can be found in [\[46\]](#).

The next steps towards finally establishing the imaging system as a reliable data acquisition and diagnostics tool will include calibration of the magnification as well as the imaging intensity in order to properly deduce the properties of the atomic clouds.

## A. Appendix

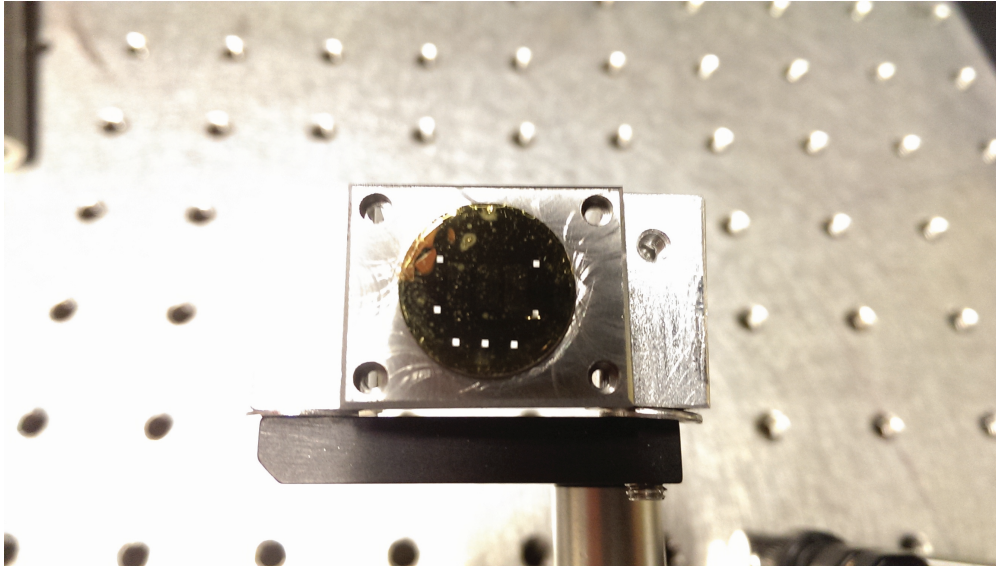


Figure A.1.: Picture of the gold grating that was used as a test pattern. Clearly visible are the rectangular holes that were used to align the position along the optical axis. The grating structure is located on the gold foil surrounded by the rectangular holes.

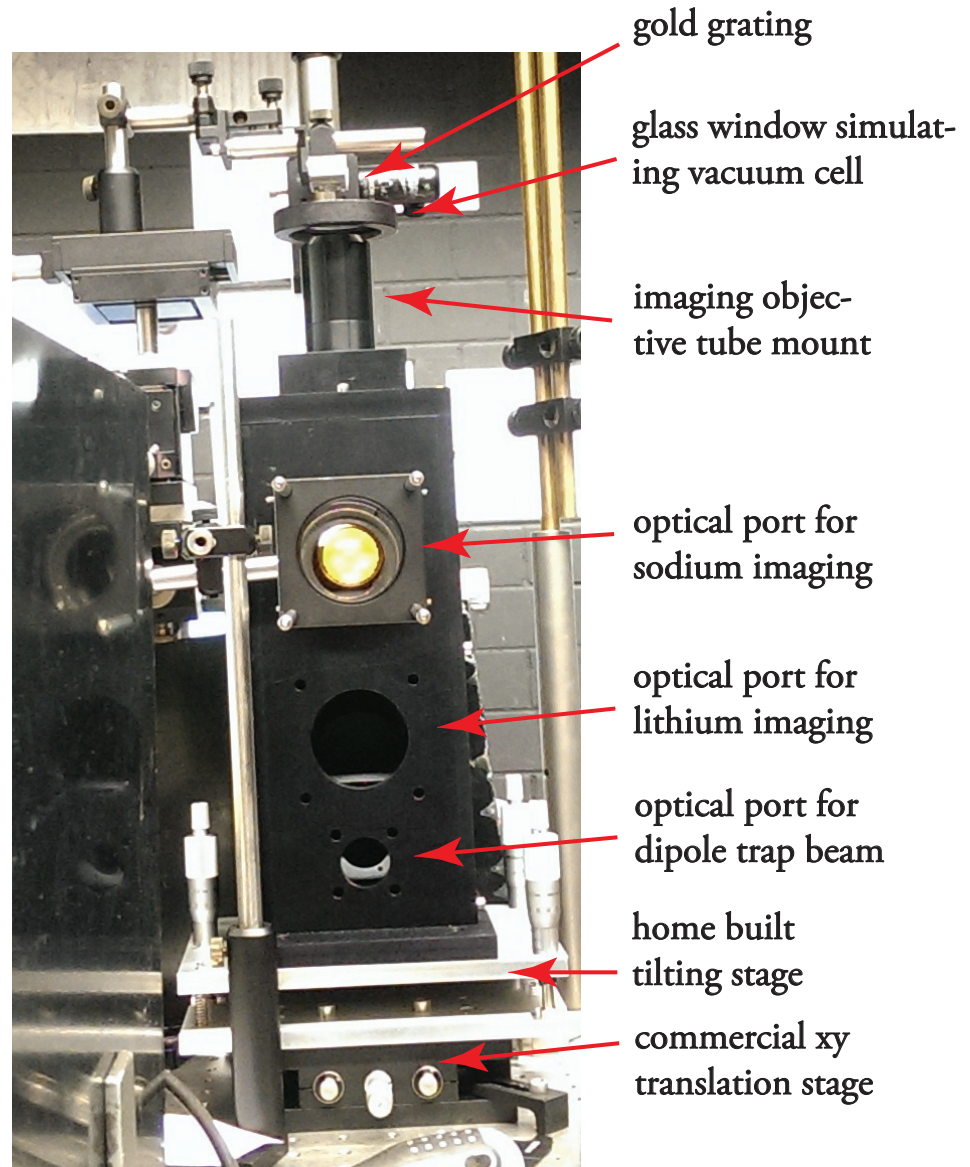


Figure A.2.: Picture of the test setup taken from the position of the sodium camera (TOWER is seen from the front). In this photograph only the secondary lens of the sodium path is mounted.

# List of Figures

2.1.	Sketch of geometrical image formation . . . . .	11
2.2.	Coordinate system for diffraction integral formula . . . . .	12
2.3.	Sketch of diffraction by means of a positive lens . . . . .	13
2.4.	Graph of Airy disc and one dimensional profile . . . . .	14
2.5.	Coordinate system for image formation formula . . . . .	15
2.6.	Graphical description of resolution according to the Rayleigh criterion . . . . .	18
2.7.	Sketch of the wavefront deviations caused by aberrations . . . . .	19
3.1.	Sketch of the vacuum cell and surrounding constructions in the experiment . . . . .	23
3.2.	Sketch of the lens design proposed by W. Alt and the final NaLi lens design . . . . .	24
3.3.	Graph showing the chromatic focal shift of the imaging objective . . . . .	26
3.4.	Sketch of the infinity corrected microscopy setup as used in the NaLi setup . . . . .	27
3.5.	Graph showing the simulated PSFs for different wavelengths and the FOV . . . . .	28
3.6.	Graph showing the effects of defocus on the PSF spot size . . . . .	29
3.7.	Graph showing the effects of defocus on the PSF peak intensity . . . . .	30
3.8.	Results of the Monte Carlo tolerancing of 100 simulated lens systems . . . . .	31
3.9.	Graph showing the dependence of the MC simulations as a function of NA . . . . .	32
3.10.	Sketch of the lens tube design . . . . .	33
3.11.	Technical drawing of the TOWER . . . . .	35
4.1.	Sketch of the setup for testing the imaging lens and TOWER . . . . .	38
4.2.	Raw images of the gold grating and a cropped region of a single hole . . . . .	40
4.3.	Influence of finite grating hole size on image evaluation . . . . .	41
4.4.	Graph showing the fitting routine for the PSF analysis . . . . .	42
4.5.	Focus scan analysis for NA = 0.41 . . . . .	43
4.6.	Focus scan analysis for NA = 0.29 . . . . .	44
4.7.	DOF as a function of NA . . . . .	45
4.8.	Resolution as a function of NA . . . . .	47
4.9.	Analysis summary FOV . . . . .	48
5.1.	First absorption images of sodium clouds . . . . .	51
A.1.	Picture of the gold grating that was used as a test pattern . . . . .	53
A.2.	Picture of the test setup from the cameras point of view . . . . .	54



# List of Tables

3.1. Table of individual lens Parameters of the imaging objective . . . . .	25
3.2. Table with the relevant imaging properties of the imaging lens design for the wavelengths of interest . . . . .	28
4.1. Summary of the experimentally determined resolution at the minimum in Figure 4.8 (NA = 0.35). . . . .	47



# Bibliography

- [1] Wolfgang Alt. “An objective lens for efficient fluorescence detection of single atoms”. In: *Optik–International Journal for Light and Electron Optics* 113.3 (2002), pp. 142–144.
- [2] MH Anderson et al. “Observation of Bose-Einstein Condensation in a Dilute Atomic Vapor”. In: *science* 269 (1995), p. 14.
- [3] MR Andrews et al. “Observation of interference between two Bose condensates”. In: *Science* 275.5300 (1997), pp. 637–641.
- [4] MR Andrews et al. “Propagation of sound in a Bose-Einstein condensate”. In: *Physical review letters* 79.4 (1997), p. 553.
- [5] Waseem S Bakr et al. “A quantum gas microscope for detecting single atoms in a Hubbard-regime optical lattice”. In: *Nature* 462.7269 (2009), pp. 74–77.
- [6] Fabian Bergermann. “Characterization of the Moire Deflectometer for the AEGIS Experiment”. Diploma Thesis, University Heidelberg, 2016.
- [7] Max Born and Emil Wolf. *Principles of optics: electromagnetic theory of propagation, interference and diffraction of light*. CUP Archive, 2000.
- [8] Kendall B Davis et al. “Bose-Einstein condensation in a gas of sodium atoms”. In: *Physical review letters* 75.22 (1995), p. 3969.
- [9] Zernike von F. “Beugungstheorie des schneidenverfahrens und seiner verbesserten form, der phasenkontrastmethode”. In: *Physica* 1.7-12 (1934), pp. 689–704.
- [10] Miroslav Gajdacz et al. “Non-destructive Faraday imaging of dynamically controlled ultracold atoms”. In: *Review of Scientific Instruments* 84.8 (2013), p. 083105.
- [11] Michael E Gehm. “Properties of  $^6\text{Li}$ ”. In: *Jetlab*, (2003).
- [12] Lens-Optics GmbH. *Bürgermeister-Neumeyr-Strasse 7 85391 Allershausen Germany*. <http://www.lens-optics.de/>. 2016.
- [13] Thorlabs GmbH. *Hans-Boeckler-Str. 6 85221 Dachau/Munich Germany*. <https://www.thorlabs.com/>. 2016.
- [14] Markus Greiner, Cindy A Regal, and Deborah S Jin. “Emergence of a molecular Bose-Einstein condensate from a Fermi gas”. In: *Nature* 426.6966 (2003), pp. 537–540.
- [15] Markus Greiner et al. “Exploring phase coherence in a 2D lattice of Bose-Einstein condensates”. In: *Physical Review Letters* 87.16 (2001), p. 160405.
- [16] Markus Greiner et al. “Quantum phase transition from a superfluid to a Mott insulator in a gas of ultracold atoms”. In: *nature* 415.6867 (2002), pp. 39–44.

## Bibliography

- [17] Diana Nyvssonen Grimes and Brian J Thompson. “Two-point resolution with partially coherent light”. In: *JOSA* 57.11 (1967), pp. 1330–1334.
- [18] Min Gu. *Advanced optical imaging theory*. Vol. 75. Springer Science & Business Media, 2000.
- [19] Eugene Hecht. *Optik. 5., verbesserte Auflage*. 2009.
- [20] Bo Huang, Mark Bates, and Xiaowei Zhuang. “Super resolution fluorescence microscopy”. In: *Annual review of biochemistry* 78 (2009), p. 993.
- [21] Ralph Jacobson et al. *Manual of Photography*. Taylor & Francis, 2000.
- [22] F Jendrzejewski et al. “Subwavelength-width optical tunnel junctions for ultracold atoms”. In: *arXiv preprint arXiv:1609.01285* (2016).
- [23] Selim Jochim et al. “Bose-Einstein condensation of molecules”. In: *Science* 302.5653 (2003), pp. 2101–2103.
- [24] V Kasper et al. “Schwinger pair production with ultracold atoms”. In: *arXiv preprint arXiv:1506.01238* (2015).
- [25] W Ketterle, DS Durfee, DM Stamper-Kurn, et al. “Making, probing and understanding Bose-Einstein condensates”. In: *arXiv preprint cond-mat/9904034* 5 (1999).
- [26] Rudolf Kingslake and R Barry Johnson. *Lens design fundamentals*. academic press, 2009.
- [27] Till Leuteritz. “High Resolution Imaging of an Ultracold Fermi Gas”. Master Thesis, University Bonn, 2016.
- [28] Stephen G Lipson, Henry S Lipson, and David S Tannhauser. *Optik*. Springer-Verlag, 2013.
- [29] A Maréchal. “Rev. d’optique 26 257 (1947). 37, 982 (1947)”. In: *J. Opt. Soc. Am* 37 (1947), p. 982.
- [30] John Medina. *Brain Rules: 12 Principles for Surviving and Thriving at Work, Home, and School*. ReadHowYouWant. com, 2011.
- [31] Wolfgang Muessel et al. “Optimized absorption imaging of mesoscopic atomic clouds”. In: *Applied Physics B* 113.1 (2013), pp. 69–73.
- [32] Kilian Muller. “Coherent transport of ultracold atoms in disordered potentials: Manipulation of time-reversal symmetry in weak localization experiments”. PhD thesis. Palaiseau, Institut d’optique théorique et appliquée, 2014.
- [33] Timo Ottenstein. “A new objective for high resolution imaging of Bose-Einstein condensates”. Diploma Thesis, Universität Heidelberg, 2006.
- [34] Lev Pitaevskii and Sandro Stringari. *Bose-Einstein Condensation and Superfluidity*. Vol. 164. Oxford University Press, 2016.
- [35] Philipp M Preiss et al. “Quantum gas microscopy with spin, atom-number, and multilayer readout”. In: *Physical Review A* 91.4 (2015), p. 041602.
- [36] Lord Rayleigh. “XXXI. Investigations in optics, with special reference to the spectroscope”. In: *The London, Edinburgh, and Dublin Philosophical Magazine and Journal of Science* 8.49 (1879), pp. 261–274.

- [37] G Reinaudi et al. “Strong saturation absorption imaging of dense clouds of ultracold atoms”. In: *Optics letters* 32.21 (2007), pp. 3143–3145.
- [38] T Rentrop et al. “Observation of the phononic Lamb shift with a synthetic vacuum”. In: *arXiv preprint arXiv:1605.01874* (2016).
- [39] Bahaa EA Saleh, Malvin Carl Teich, and Bahaa E Saleh. *Fundamentals of photonics*. Vol. 22. Wiley New York, 1991.
- [40] R Scelle et al. “Motional coherence of fermions immersed in a Bose gas”. In: *Physical review letters* 111.7 (2013), p. 070401.
- [41] Friedhelm Serwane. “Deterministic preparation of a tunable few-fermion system”. PhD thesis. University of Heidelberg, 2011.
- [42] Jacob F Sherson et al. “Single-atom-resolved fluorescence imaging of an atomic Mott insulator”. In: *Nature* 467.7311 (2010), pp. 68–72.
- [43] Daniel A Steck. “Sodium D line data”. In: *Report, Los Alamos National Laboratory, Los Alamos* 124 (2000).
- [44] Christian Steinhauer et al. “Superresolution microscopy on the basis of engineered dark states”. In: *Journal of the American Chemical Society* 130.50 (2008), pp. 16840–16841.
- [45] TG Tiecke. “Properties of potassium”. In: *University of Amsterdam, The Netherlands, Thesis* (2010), pp. 12–14.
- [46] Arno Trautmann. “Spin Dynamics and Feshbach Resonances in Ultracold Sodium-Lithium Mixtures”. PhD thesis. University of Heidelberg, 2016.
- [47] Mankei Tsang, Ranjith Nair, and Xiaoming Lu. “Quantum theory of superresolution for two incoherent optical point sources”. In: *arXiv preprint arXiv:1511.00552* (2015).

*Bibliography*

Erklärung:

Ich versichere, dass ich diese Arbeit selbstständig verfasst habe und keine anderen als die angegebenen Quellen und Hilfsmittel benutzt habe.

Heidelberg, den 15.09.2016

.....